Received: 11 December 2020 | Revised: 11 March 2021 | Accepted: 15 March 2021

DOI: 10.1002/dep2.143

ORIGINAL RESEARCH ARTICLE

The Depositional Record Open Access
A journal of the International Association of Sedimentologists
WILEY

The fate of a travertine record: Impact of early diagenesis on the Y-10 core (Mammoth Hot Springs, Yellowstone National Park, USA)

Eva De Boever[1,2] | **David Jaramillo-Vogel**[1,3] | **Anne-Sophie Bouvier**[4] | **Norbert Frank**[5] | **Andrea Schröder-Ritzrau**[5] | **Lukas Baumgarter**[4] | **Rudy Swennen**[6] | **Anneleen Foubert**[1]

[1]Department of Geosciences, University of Fribourg, Fribourg, Switzerland

[2]TNO, Geological Survey of the Netherlands, Utrecht, the Netherlands

[3]Particle Vision GmbH, Fribourg, Switzerland

[4]Institute of Earth Sciences, University of Lausanne, Lausanne, Switzerland

[5]Institute for Environmental Physics, University of Heidelberg, Heidelberg, Germany

[6]Department of Earth and Environmental Sciences, KU Leuven, Leuven, Belgium

Correspondence
Eva De Boever, Department of Geosciences, University of Fribourg, Fribourg, Switzerland.
Emails: eva.deboever@tno.nl; eva.deboever@unifr.ch

Funding information
Total, Grant/Award Number: Project n_FR5585; Schweizerischer Nationalfonds zur Forderung der Wissenschaftlichen Forschung, Grant/Award Number: 154810 QuantiCarb@Spring and 4D-Diagenesis@Mound (SNSF grant 200021_14924)

Abstract

Spring systems are efficient and fast precipitating non-marine carbonate factories, but they are also prone to (early) diagenesis. Evidence of diagenesis in travertines remains controversial as the resulting textures have been considered primary in other deposits and the impact on geochemical/palaeo-environmental signals is often poorly addressed. This study revisits the Y-10 core, taken in 1967 at one of the upper terraces of Mammoth Hot Springs in Yellowstone National Park (USA). The travertine depositional facies in the upper 50 m of the core show a general distal to proximal facies trend upwards. To unravel the nature, impact and timing of early diagenesis, fabrics and geochemical signatures are also compared to modern hot spring carbonates. Secondary ion mass spectrometry and detailed microscopy proved powerful in determining the stable isotope signature of different cement generations, thereby detangling the fluid history. Diagenesis starts during spring activity, but these warm waters not only precipitate $CaCO_3$ at the top, they also seem to have circulated through the porous spring fabrics below. It resulted in coarsening and homogenization of the primary textures through neomorphism of aragonite and calcite cementation, often resulting in new intracrystalline microporosity within the calcite crystals. Subsequent circulation of meteoric fluids led to dissolution and cementation, particularly near the top of the core. Careful interpretation of U/Th dates suggests that travertine deposition started at the beginning of the Holocene/end Pleistocene. Calculated depositional (precipitation) rates vary between 2 and 20 mm/year, assuming a constant rate between samples at different depths. Aragonite deposits are completely transformed to calcite below depths of 5–10 m, corresponding to a time span of 4,000 years. Core and petrography observations, together with dating, suggest that travertine strata below marine sandstones in the lower part of the core may relate to fault displacement after the onset of travertine deposition.

KEYWORDS
calcium carbonate, diagenesis, hot spring, SIMS

1 | INTRODUCTION

The Y-10 core, drilled in 1967 by the United States Geological Survey (USGS), shows a 113 m long record of hot spring carbonate deposition covering Mesozoic sediments at Mammoth Hot Springs (MHS) in the north of Yellowstone National Park (YNP; Wyoming-Montana, USA). It was drilled with the goal to obtain information on the history of hot spring activity and on the subsurface hydrothermal conditions (White et al., 1975). Today it offers a unique and continuous record of the history of hot spring carbonate deposition and the impact of early diagenesis within a still active terrestrial (hot) spring system.

Spring carbonates precipitate and form centimetre to hundreds of metre-scale deposits in the outflow of terrestrial springs. These fluids are characterised by a high concentration of dissolved Ca^{2+} and carbonate species (Brasier, 2011; Jones & Renaut, 2010; Pentecost, 2005). A continuum exists in springs in terms of water temperature and water chemistry, rock facies, fabrics and microbial or biological signatures (Arp et al., 2010; Okumura et al., 2012, 2013; Pentecost, 2005; Shiraishi et al., 2008). The deposition of (mostly) calcium carbonates results from the interplay of physicochemical processes (CO_2 degassing, flow turbulence) and the presence (nucleation templates) and activity of (sulphate reducing, photosynthetic; micro)biota (Andrews & Brasier, 2005; Bissett et al., 2008; Pentecost, 2005; Takashima & Kano, 2008). Studying spring carbonate depositional processes will help us understand the preservation and/or alteration of these typically laminated, potential palaeoenvironmental and palaeoclimate records (Andrews & Brasier, 2005; Brasier et al., 2010; Kano et al., 2003; Rodríguez-Berriguete et al., 2018). Furthermore, the high rates of carbonate precipitation (0.2–1.0 mg/cm^{3}h at MHS, Fouke, 2011) makes the study of carbonate depositional processes in these settings relevant for different engineering and geotechnical applications (clogging of filters and wells in (geo)thermal installations, CO_2 storage; Boch et al., 2017; Zhang et al., 2018). Finally, non-marine spring carbonates may contain preserved 'biomarkers' making them relevant archives to study and reconstruct potential ancient life assemblages (Brasier et al., 2011, 2015; Peng & Jones, 2013).

Many travertine studies focussed on the sedimentological architecture and large-scale geometry of continental spring carbonate bodies, as well as on the classification of common fabrics/facies, to determine their depositional conditions and controls and thus infer the evolution of ancient spring systems (Brogi et al., 2009; Claes et al., 2015, 2017; De Boever et al., 2017b; Della Porta, 2015; Della Porta et al., 2017; Gandin & Capezzuoli, 2014; Guo & Riding, 1998, 1999; Lopez et al., 2017; Sharp et al., 2013; Török et al., 2016). The rapid lateral and vertical alternations and changes in facies and fabrics, at multiple scales, are causes of their heterogeneity and anisotropy in petrographic and geophysical properties (Claes et al., 2017; De Boever et al., 2016; Gagrcía-del-Cura et al., 2012; Soete et al., 2015). Gradually, interest in the presence and variety of diagenetic products in calcareous spring deposits increased (Arp et al., 2013; Claes et al., 2017; Gandin & Capezzuoli, 2014; Rodríguez-Berriguete, 2020; Shiraishi et al., 2020). The processes and their products go beyond localised precipitation of cements in cavities/fractures, or dissolution by meteoric waters, resulting in enlarged voids. Diagenesis in these settings may result in textures and microscopic fabrics (microfabrics) that are considered primary in other settings (Frisia et al., 2018), adding to the confusion of how to interpret them and the physicochemical and depositional context in which these deposits initially formed (Brasier et al., 2011; De Boever et al., 2017a). A number of case studies have suggested that diagenesis starts early and proceeds fast in non-marine carbonates (Chafetz et al., 1994; Golubić et al., 2008; Janssen et al., 1999; Rainey & Jones, 2007), although the exact rates are hard to define (Andrews & Brasier, 2005; Arp et al., 2001; Pederson et al., 2020; Shiraishi et al., 2020). Finally, the impact of early diagenetic processes on the preservation of elemental and isotopic signals used in palaeo-environmental reconstructions (Andrews, 2006; Andrews & Brasier, 2005; Brasier et al., 2010; Takashima & Kano, 2008), and in particular the dating of palaeoclimate records, is an important although still controversial topic in non-marine carbonate research (Falk et al., 2016; Frisia et al., 2018; Kele et al., 2003; Pederson et al., 2019; Scholz et al., 2014; Zhang et al., 2014).

Diagenesis of travertine fabrics in the Y-10 core is macroscopically obvious (Chafetz & Guidry, 2003), but the core section also offers a unique view into the intermediate steps of fabric changes at a site of active hot spring activity and ongoing travertine deposition. It further allows the concurrent impact of these processes on the stable isotopic signature of the calcium carbonate phases to be assessed. Following an overview study of the core by Chafetz and Guidry (2003), this study aims to revisit the evolution of travertine facies in the Y-10 core and, in particular, to:

- Address processes and drivers of early diagenesis.
- Assess the time frame of travertine deposition and diagenesis.

The results presented here may prove relevant towards the palaeoclimate and palaeo-environmental interpretation of other Quaternary records of non-marine (spring) carbonates.

2 | GEOLOGICAL SETTING

2.1 | Regional geology and stratigraphy

Yellowstone National Park hosts numerous hot springs, geysers, fumaroles and mud pots that are heated by the

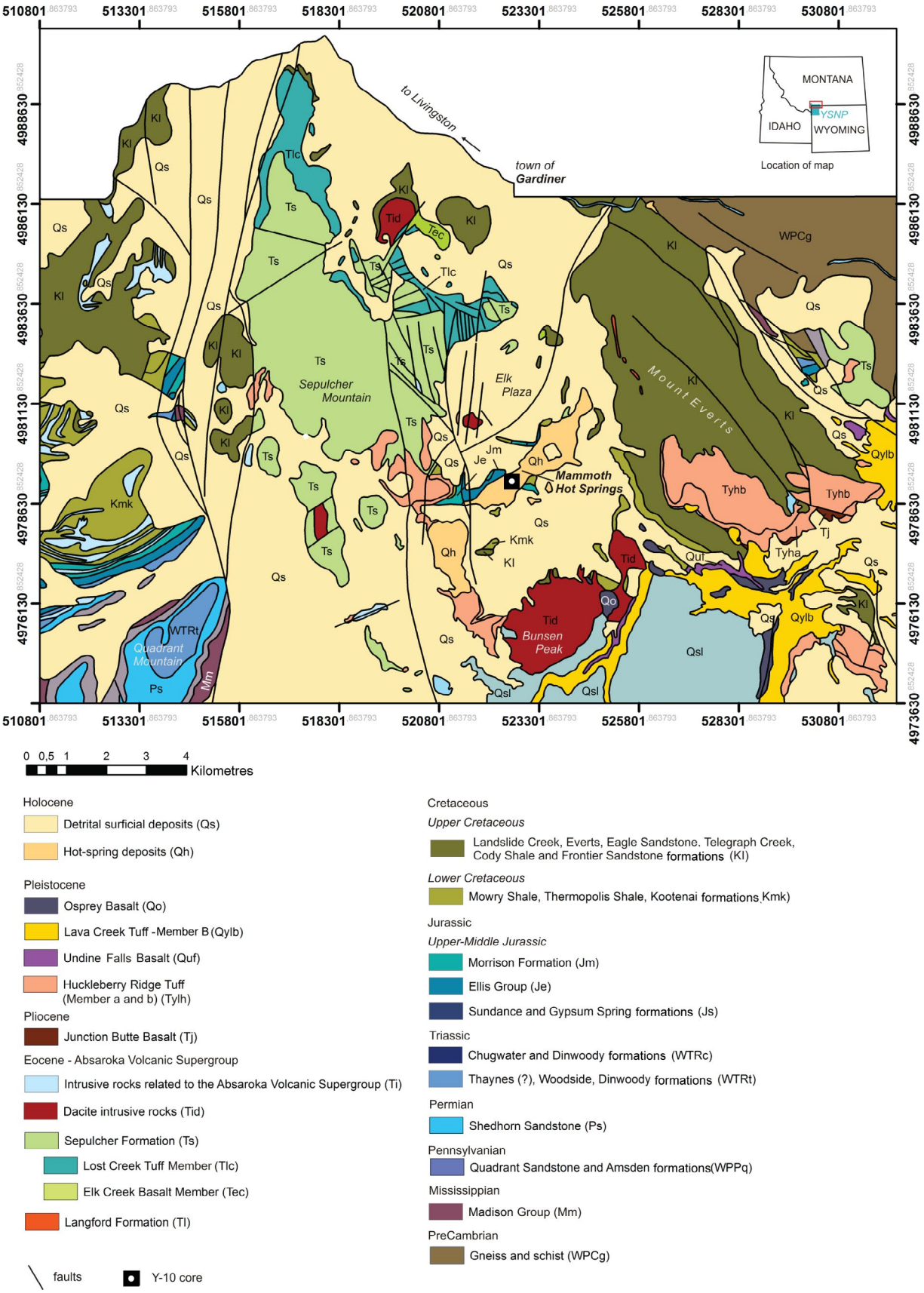

FIGURE 1 Geological map of the northern part of Yellowstone National Park with the location of Mammoth Hot Springs and the Y-10 core (WY, USA). Modified after Christiansen (1999)

Yellowstone supervolcano (Rye & Truesdell, 2007). The MHS Complex is located in the subsiding Norris-Mammoth Corridor in the northern part of the Park (Figure 1). This corridor is a north-south alignment of volcanic vents and areas of hydrothermal activity outside the Yellowstone caldera. The Yellowstone caldera (50 × 80 km in diameter), which formed 640,000 years before present (ybp), is floored by an upper silicic magma chamber that provides both heat and CO_2-rich waters to the hydrothermal system (Lowenstern & Hurwitz, 2008).

Stratigraphically, the spring deposits overlay a thick sequence of Palaeozoic to Mesozoic marine and non-marine sandstones, conglomerates, shales and limestones (Bargar, 1978). From Cambrian through Triassic times, the area was relatively stable. Important carbonate deposits are the Carboniferous marine limestones and dolostones of the Madison Group (thickness of 396.2 m; Ruppel, 1982). The Triassic section in the northern part of YNP consists of a light grey to brown, fine-grained, calcareous sandstone (Thaynes Formation, 3–4.5 m; Ruppel, 1982). Jurassic through Cretaceous times are characterised by sedimentation in the shallow Rocky Mountain depression with depositional environments ranging from shallow oceans to swamps and river flood plains (Bargar, 1978; Fraser et al., 1969; Ruppel, 1982). Deposits include the Middle to Upper Jurassic marine sediments of the Ellis Group (Sawtooth Formation: 32–47 m thick, Rierdon Formation: 12–18 m thick and Swift Formation: 4.5–18 m thick). They are overlain by non-marine shale to siltstone beds of the Upper Jurassic Morrison Formation (around 60 m thick; Ruppel, 1982). Rocks of Cretaceous ages form a relatively thick sequence of up to 1,219 m. The last evidence of marginal marine layers is found in localised beds in the Upper Cretaceous Eagle Sandstone and Everts Formations. The overlying conglomeratic sandstones, mud and claystones reflect fluvial deposition (Fraser et al., 1969). Deposition ended with the Laramide orogeny (late Cretaceous–early Eocene). The latter resulted in uplift, deep erosion (Fraser et al., 1969) and a pattern of north-east and north-west trending, high-angle faults creating a mosaic of uplifted blocks.

The Tertiary, between 1.2 and 0.16 Ma, is marked by several periods of volcanic activity with deposition of the Absaroka Volcanic Supergroup lava in the late Eocene and several basalt and tuff deposits from the Yellowstone caldera during the Pleistocene (Fraser et al., 1969). Besides volcanic activity, three periods of glaciations mark the Pleistocene, namely: the pre-Bull Lake (300 to 180 ka), the Bull Lake (170 to 125 ka) and the Pinedale glaciations (47 to 13 ka; Fraser et al., 1969). Stratigraphic field relationships show that travertine deposits in the Gardiner area locally overlay and thus post-date Bull Lake glacial deposits (Fraser et al., 1969; Sturchio et al., 1994). Uranium-series ages published by Sturchio et al. (1994) suggest that travertine deposition partly overlaps with the Pinedale glacial episode and coincides with periods of glacier retreat. The travertine deposits of MHS are not covered by any glacial deposits and would thus post-date the last glacial events in the area. An U-Th age of 28 years was determined for sub-Recent travertine of the Liberty Cap at MHS and a sample at 2.4 ft (0.73 m) in the Y-10 core was dated at 37 years (Sturchio, 1990) using U/Th and ^{226}Ra.

2.2 | Mammoth Hot Springs

The vents at MHS expel Ca-Na-HCO_3-SO_4-type CO_2-rich waters (Bargar, 1978). Maximum temperature is 73°C (White et al., 1975) and spring waters emerge with a pH of 6 (Kharaka et al., 2000; Sorey & Colvard, 1997), evolving to ambient temperatures and a pH of 8 towards the distal portions of the spring system (Fouke, 2011; Fouke et al., 2000; Veysey et al., 2008). The spring waters are derived from meteoric water in the Gallatin Mountain Range that infiltrated and migrated through the subsurface along faults and fractures allowing mixing with a magmatic-derived water source (Kharaka et al., 2000; Rye & Truesdell, 2007). The MHS spring water and travertine $\delta^{34}S$ and $^{87}Sr/^{86}Sr$ values suggest subsurface water–rock interaction at about 100°C with the Mississippian-age limestone and evaporite deposits of the Madison Group (Kharaka et al., 1991; Rye & Truesdell, 2007; Sorey & Colvard, 1997).

In the active MHS system, a sequence of five travertine facies is described along the primary spring outflow path (Fouke, 2011; Fouke et al., 2000; Veysey et al., 2008; Figure 2A,B). The facies succession includes the Vent (V), Apron and Channel (AC), Pond (P), Proximal Slope (PS) and Distal Slope (DS). It consistently forms downstream as the spring water rapidly cools, degasses CO_2 and precipitates travertine. Specific microbial communities are associated with each facies (Fouke et al., 2003). Travertine mineralogy in the Vent and Apron-Channel facies is dominantly aragonite. Downstream, towards the Distal Slope, increasing amounts of calcite are found.

The macrofabrics and microfabrics in active springs have been described and illustrated by Fouke (2011) and Fouke et al. (2000). In Recent deposits, the recurring texture is an aggregation of fine aragonite needles, 20–100 μm long. Depending on the depositional facies, they are organised in different ways leading to different microfabrics, as described below.

In the streamer deposits of the Apron-Channel Facies (Fouke, 2011), aragonite needles form splays that radiate outward around a central, microbial filament. Between the encrusted filaments, mineralized extracellular polymeric substances (EPS) are observed (Figure 3A). Aragonite needles, stacked in loosely packed, shrub textures (Chafetz & Guidry,

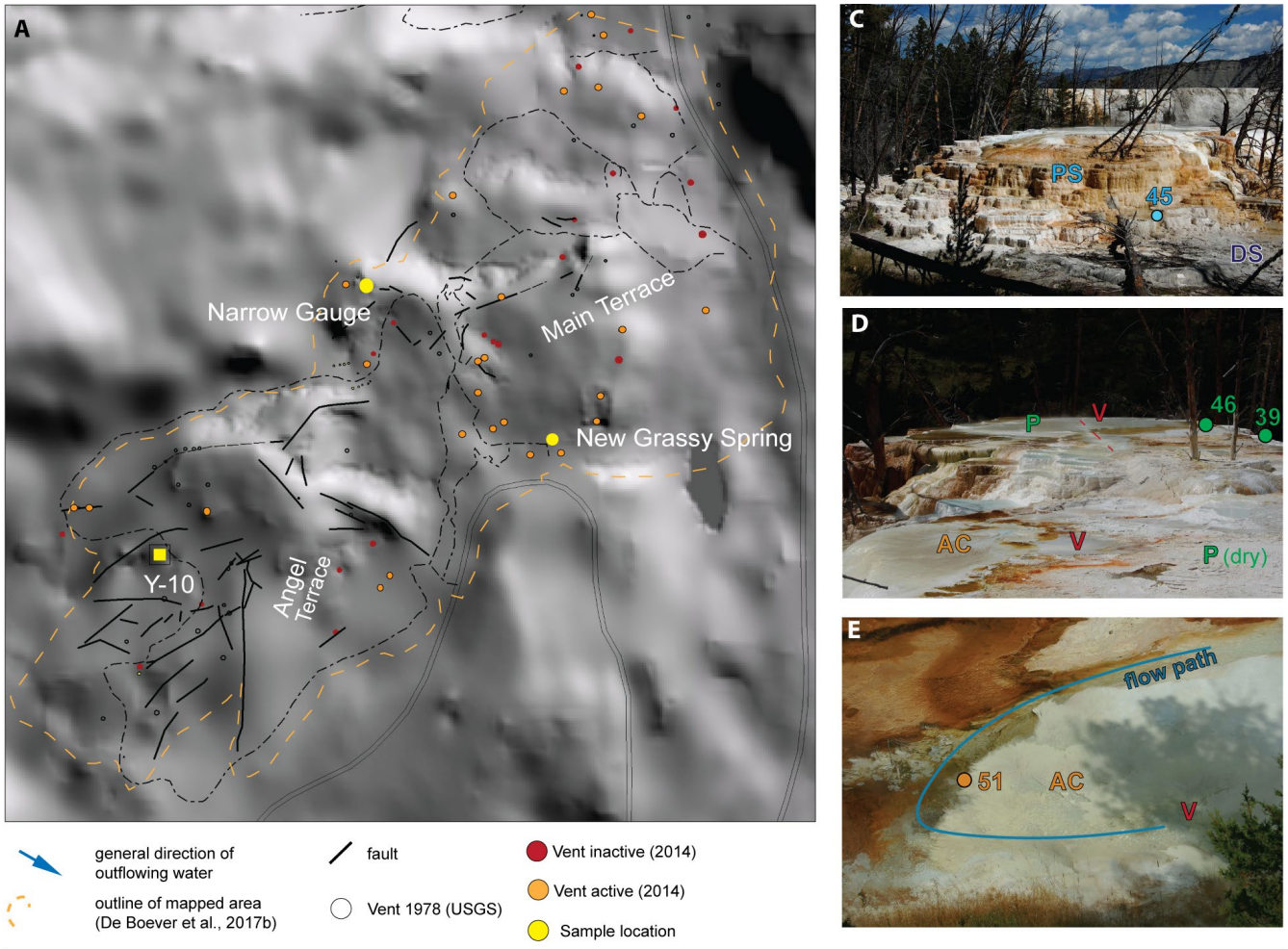

B

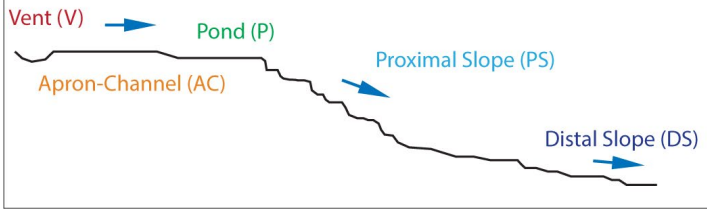

sample(s)	spring	loc.	Facies	pH	T (°C)
YS01, 02, 06, 14	Narrow Gauge	dry	PS		
YS04	Narrow Gauge	dry	AC		
YS39	Narrow Gauge	dry	P		
YS45	Narrow Gauge	active	PS to DS	7.75	43.8
YS46	Narrow Gauge	dry	P		
YS50	Narrow Gauge	active	DS	8.30	25.8
YS51	New Grassy Spring	active	AC to P	7.32	51.6

FIGURE 2 Study locations and facies at Mammoth Hot Springs (MHS). (A) Shaded topography map of MHS indicating the sampled springs and location of the Y-10 core. (B) Sample table and a schematic downstream facies transect according to the five-fold facies scheme of Fouke et al. (2000). Sample location (loc.): dry = outflow path was dry at the moment of sampling. Active = outflow path with flowing water at the moment of sampling. V = Vent, AC = Apron and Channel, P = Pond, PS = Proximal Slope and DS = Distal Slope. Images illustrates the different facies and some of the sample spots at the modern springs. Sample locations (dots) and numbers are coloured according to the facies. (C) Front view of Narrow Gauge spring. (D) Top view of Narrow Gauge spring. (E). Outflow path of New Grassy spring

2003; Fouke et al., 2000; Pentecost, 1990) and in dumbbell-shaped aggregates (10–50 μm across), are typical building components of coated bubbles, peloids, aragonite rafts and the laminated deposits in the Pond Facies.

In the following, the term shrub or shrub texture is used to refer to nested splays of (aragonite) needles that radiate outward and are stacked forming bushes (Jones, 2017), typical of the MHS deposits (Chafetz & Guidry, 2003; Fouke et al., 2000; Pentecost, 1990). In other hot spring deposits, these bush-like textures, called shrubs, may have a micritic or (clotted) peloidal microfabric (Della Porta, 2015; Gandin & Capezzuoli, 2014). Dendrites or dendritic textures (Jones, 2017) refer to branching, often complex, crystal aggregates. They may have a range of crystal and branching morphologies (Claes et al., 2017; Gandin & Capezzuoli, 2014; Jones, 2017; Jones & Peng, 2012; Jones & Renaut, 2008; Rodríguez-Berriguete, 2020) that sometimes have been given specific, morphological names (dendritic fan, band and feathers; Della Porta, 2015; Gandin & Capezzuoli, 2014; Jones & Renaut, 2008).

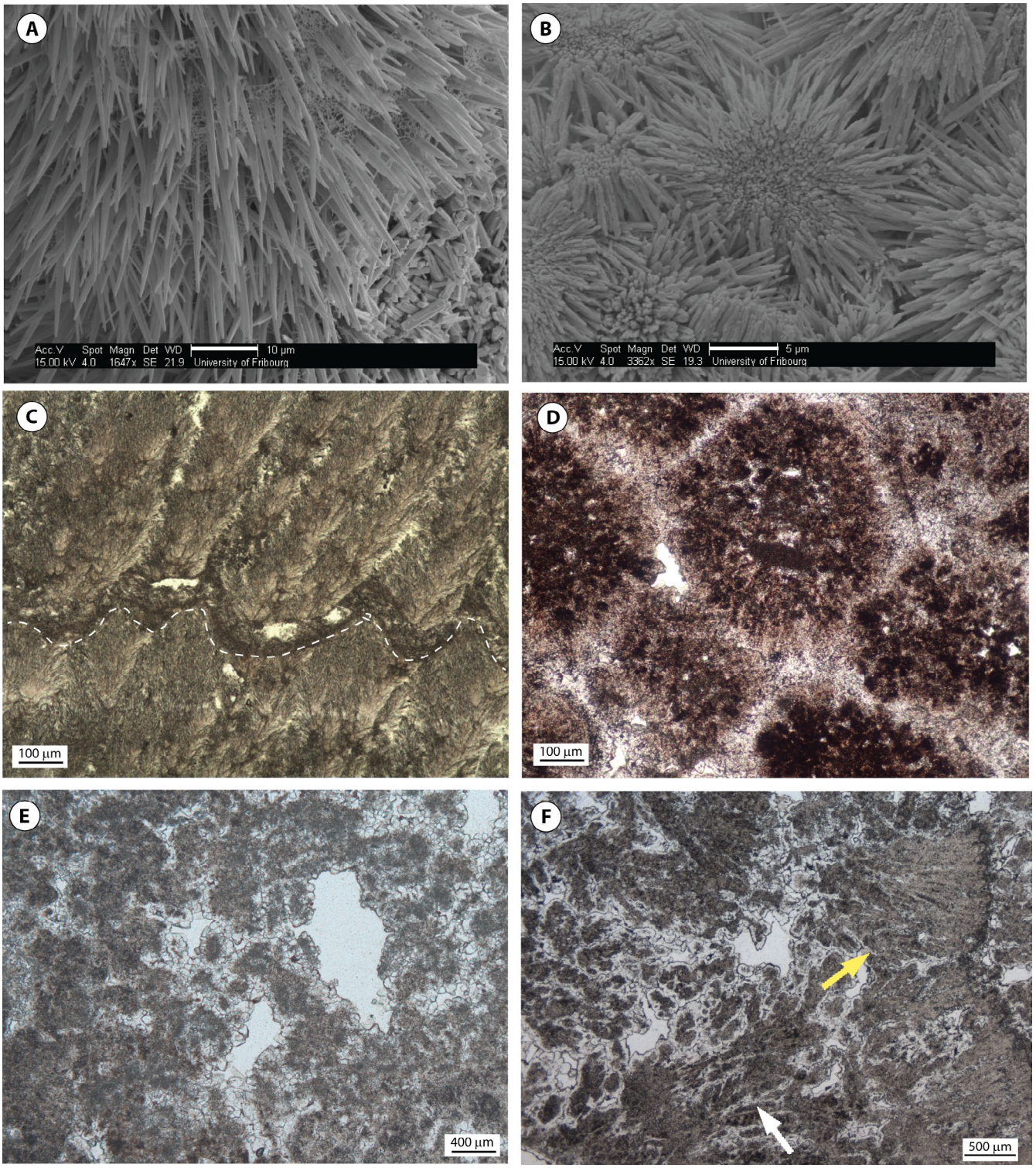

FIGURE 3 Petrography of modern and fossil travertine deposits. (A) Aragonite needles radiating out from a fossilized microbial filament in the Apron-Channel facies at New Grassy spring. Between the needles, fossilized EPS can be seen that connects the needles and forms a honeycomb network (SEM-SE). (B) Fine aragonite needles forming spherules in a Distal Slope sample at Narrow Gauge spring (SEM-SE). (C) Transmitted light image of aragonite shrub textures in a Proximal Slope sample from the Narrow Gauge spring. The dotted line outlines a microterracette front with some silt-sized grains deposited along it. (D) Transmitted light image of spherules in a Distal Slope facies section of the Y-10 core (sample 27). (E) Transmitted light image of micritic to peloidal fabric, surrounded by a transparent calcite cement rim that occurs together with the spherules of image D (Y-10, sample 27). (F) Different dendritic textures co-occurring in a Proximal Slope sample. Poorly branching dendritic textures on the left (white arrow) give way to more crystal ray fans to the right (yellow arrow; Y-10, sample 37)

High-angle surfaces on the Proximal Slope are composed of $CaCO_3$ needles that build short and more elongated shrub textures (Figure 3C), but may also consist of $CaCO_3$ branching dendritic textures (Della Porta, 2015), resembling feathers or radiating crystal fans (Della Porta, 2015). The 'microterracettes' that characterise the face of some of the terraced slope deposits correspond to variations in the length of the shrubs (Figure 3C). In places, the wavy appearance of the microterrace front is accentuated by the presence of silt-sized grains and micrite (Figure 3C). Radial outgrowing, aragonite crystal bushes forming spherical masses called 'spherules' by Fouke et al. (2000), typify the Distal Slope facies deposits (Figure 3B). Feather calcite crystal aggregates are observed in both facies and often co-occur with diatom frustules and calcified filaments.

2.3 | The Y-10 core

The Y-10 core (Lat: 44.97–Lon: −110.71; Figure 2A) is located in the upper terrace, just off the boardwalk (White et al., 1975). During drilling, CO_2 was found to be in solution below a depth of 51.8 m (170 ft). Below 57.9 m (190 ft), drilling problems occurred with loss of material and reduced recovery. This was most prominent between depths of 79.8 and 98.1 m (262 and 322 ft) in Mesozoic rocks (Cretaceous or Jurassic). Work by Sturchio (1990) report clastic interlayers, glacial till and Mesozoic basement between and below the travertine rocks. These deposits were interpreted as volcanoclastic sediments in the study of Chafetz and Guidry (2003).

Previous sedimentological and diagenetic work on the Y-10 core sediments was published by Chafetz and Guidry (2003), who presented the first lithological overview and a detailed description of the micro-travertine and macro-travertine fabrics. They report two episodes of travertine accumulation, intercalated with 'volcanoclastic deposits'; one accumulation preserved between 67 and 60 m and the main travertine accumulation from 50 m depth to the top of the core. In this study, the two episodes are referred to as the lower and the upper continuous travertine section, respectively. With the presence of scarce ostracod carapaces, among other criteria, the lower section was interpreted as deposition within a lacustrine environment, whereas the upper 40 m of the core points to the development of a terraced mound system. The authors also recognise the importance of extensive dissolution and the precipitation of secondary cements (Chafetz & Guidry, 2003). Their large dataset of stable carbon and oxygen isotopes shows some positive correlation of $\delta^{13}C$ and $\delta^{18}O$ values, which was interpreted to result from a change in depositional environment from more distal at the base to more proximal, closer to the vent, at the top, either by progradation of the system or a change in the vent position. However, other effects such as changes in fluid composition and temperature during deposition are not excluded (Chafetz & Guidry, 2003).

3 | MATERIAL AND METHODS

3.1 | Field sampling and core logging

Modern travertine samples at MHS were collected at Narrow Gauge Springs and New Grassy Springs in 2014 (Figure 2C–E). Freshly precipitated travertine is fragile and unconsolidated. Very small centimetre-sized specimens were obtained with sterile gloved hands and sterilised spatulas and knives (Fouke et al., 2000). They were transported in aluminium foil and boxes.

The Y-10 core was examined in the Core Repository Centre (CRC) of the USGS in Denver (USA). The original core has a total length of 113 m and has been cut in two halves. Only one half of the core sections is stored and accessible at the CRC (Library number D577; https://my.usgs.gov/crcwc/core/report/11629). The core has a width of 10 cm at the top, decreasing to 4.5 cm at the base. All studied core sections were photographed and the lithology was described with the help of a hand lens. Special attention was paid to travertine and non-travertine macrofabrics and facies, and to the type and degree of diagenesis. Sample locations were selected based on core descriptions and the identification of different fabrics. Small rock chips (maximum one third of the core width at the corresponding core depth) were cut from the core by the CRC Denver staff. The small rock chips were used for thin section preparation, description of the mineralogy, stable C and O isotope analysis and U/Th dating.

3.2 | Low-resolution to high-resolution microscopy

Recent travertine samples are often soft and friable. All samples were therefore double impregnated under low vacuum (≤0.1 mbar) with a transparent resin (Araldite XW396, Araldite DY026SP + hardener XW 397) prior to thin section preparation. Conventional transmitted light microscopy of thin sections, using a Leica DM4500 P optical microscope, allowed the microscopic fabric (microfabrics) and pore space to be examined and documented in 2D at micron scale. A Cambridge CLmk3A stage coupled to a Nikon microscope (Nikon Corporation) was used for cold cathodoluminescence (CCL) observations (University of Fribourg, Switzerland). Operating conditions were between 8.5 to 10 kV and 450 to 680 μA, 0.05 Torr vacuum. High-resolution observations of millimetre-sized pieces of Y-10 core samples and fresh, but dry, hot spring carbonate samples were performed with scanning electron microscopy (SEM). Samples were

fixed on stubs with carbon glue and gold-coated (40 nm) for observation with the FEI XL30 Sirion FEG instrument at the Department of Geosciences (University of Fribourg, Switzerland). Observations were made using the secondary electron (SE) and backscatter (BSE) detector, and images were taken using the AztecOne software (3.3 SP1, Oxford Instruments Nanotechnology Tools Lmt.). Specific working conditions are reported in figure captions.

In the following, neomorphism, following Folk (1965), refers to transformations through dissolution–reprecipitation between one mineral and a polymorph that takes place in the presence of a fluid (Dickson, 1978; Flügel, 2004). Neomorphism has a tight association with the transformation of aragonite to calcite, a process frequently reported to affect primary carbonate precipitates in non-marine settings (De Boever et al., 2017a). Alternatively, the broader term polymorphic transformation could be used. In case the transformation involves only a change in mineral form (shape and size) without changing the mineral species or composition, recrystallization is the preferred term (Dickson, 1978; Folk, 1965).

3.3 | X-ray diffractometer

The mineralogy of bulk sample powders was determined by X-ray diffractometer (XRD) at the Department of Geosciences (University of Fribourg) using a Rigaku Ultima IV diffractometer equipped with a D/teX detector (Rigaku Corporation) and a Cu X-ray tube operated at 40 kV and 40 mA. Acquisition conditions were 1°/min in steps of 0.02° between 5° and 60°. Mineral identification was performed with the PDXL2 software of Rigaku, and Rietveld refinement was conducted using the Topas software (Bruker AXS, version 5). The latter allowed the lattice parameters to be refined, the temperature factor to be taken into consideration and to account for the preferred orientation of calcite {1 0 4} and a polynomial background correction.

3.4 | Stable carbon and oxygen isotopes

3.4.1 | Bulk powder analysis

Bulk powders (10 mg) for stable carbon and oxygen isotope analysis of the macrofabrics in the different facies were obtained using a handheld Dremel Multipro Model 225 drill burr (0.25 mm diameter) composed of diamond-coated carbide steel. The same sample chips were used to obtain the XRD powder samples. The stable isotopic signatures were determined at the Friedrich-Alexander-Universität (Erlangen-Nürnberg, Germany). Carbonate powders are reacted with 100% phosphoric acid at 70°C in a Gasbench II, connected to a Thermo Finnigan Five Plus mass spectrometer (MS). All values are reported in per mil (‰), relative to the Vienna Pee Dee Belemnite (V-PDB) by assigning a $\delta^{13}C$ value of +1.95‰ and a $\delta^{18}O$ value of −2.20‰ to the standard NBS-19. Reproducibility for the $\delta^{13}C$ and $\delta^{18}O$ values are a maximum of 0.06‰ and 0.05‰, respectively.

3.4.2 | Secondary ion mass spectrometry analyses

Micro-SIMS (secondary ion mass spectrometry) spot analyses for $\delta^{13}C$ and $\delta^{18}O$ were conducted at the Centre for Advanced Surface Analyses (CASA, Lausanne, Switzerland). Polished thin sections were cut around areas of interest and pressed into indium, together with an in-house calcite standard (UNIL_C1, $\delta^{18}O$ = 18.29‰ ± 0.07 1SD V-SMOW; $\delta^{13}C$ = 0.64‰ ± 0.04 1SD V-PDB). The thin section fragments were photographed using transmitted, incident and cathodoluminescence light to allow for careful positioning of the spots to be analysed.

Oxygen and carbon isotopes were measured using a CAMECA IMS 1280HR SIMS at the SwissSIMS facility (University of Lausanne, Switzerland). A 10 kV, *ca* 1.5 nA high-density primary beam of $^{133}Cs^+$ ions in Gaussian mode was focussed with *ca* 15 μm diameter spot size on the sample surface. An electron gun was used to compensate for charge building. The secondary ions were collected simultaneously by two Faraday cup detectors (L'2 and H'2), L'2 was assigned to a $10e^{10}\Omega$ resistor for $\delta^{18}O$ measurements, and a $10e^{11}\Omega$ resistor for $\delta^{13}C$ measurements. Mass resolving power ($m/\Delta m$) was set to 2,460 for ^{18}O and ^{16}O (entrance slits were set at 122 μm and multicollection slit 1) and 4,400 for ^{12}C and ^{13}C (entrance slits at 61 μm and multicollection slit 2). The field aperture was closed to 4,000 μm and the energy slit was set to 50 eV. For $\delta^{18}O$ measurements, a pre-sputtering time of 30 s was applied, followed by automated secondary beam centring and 20 cycles of 5 s data acquisition. A slightly different analytical condition was used to measure $\delta^{13}C$ values, done in separate sessions, with 45 s pre-sputtering time, automated secondary beam centring and 20 cycles of 8 s data acquisition.

Typical *ca* 12-h sessions started with calibration of the background of the two Faraday cups and a mass calibration. The magnetic field was stabilised using the nuclear magnetic resonance probe of the 1280HR. Each session started with eight analyses of the calcite standard. The standard was also measured repeatedly (after every 8–12 sample spots), in order to monitor possible instrumental drift. Standard reproducibility at the beginning of each $\delta^{18}O$ session was *ca* 0.3‰, similar to the reproducibility of the standards (2SD) over the entire session. For $\delta^{13}C$, the standard reproducibility at the beginning of the session on eight analyses was *ca* 1‰, and

over the whole session 2–3‰ (2SD). A linear correction of the drift was applied for each $\delta^{13}C$ session. Unknown carbonate samples were corrected for machine drift and instrumental mass fractionation (=true value of the standard-drift corrected value of the standard).

Samples were occasionally partly lost or broken during preparation as a result of pressing the samples and standard within the indium or due to instability and charging during analysis. As a result, the spots for $\delta^{13}C$ and $\delta^{18}O$ analyses were not always located at exactly the same place, but in adjacent crystals with the same petrographic properties.

3.5 | ^{230}Th/U dating

Uranium-series dating was performed at the Institute for Environmental Physics at Heidelberg University. Small amounts of bulk powder (54–115 mg) were used for dating purpose. Six powder samples (YS03, YS04, YS22, YS28, YS32 and YS36) and two small carbonate pieces (replicates for travertine samples YS28 and YS36) were processed according to preparation and measurement protocols described in Douville et al. (2010) and Wefing et al. (2017). Thorium and uranium separation and purification are based on ion exchange processes using UTEVA resin following sample dissolution in nitric acid. For the replicate analysis of travertine samples YS28 and YS36, small carbonate slabs were processed according to the above-mentioned methods. The carbonate pieces were leached and separated from particulate, detrital material by centrifuging the dissolved sample. Subsequently, isotope ratios were measured using multi-collector inductively coupled-plasma mass spectrometry (MC-ICPMS, Thermo Scientific Neptune Plus) closely following the procedure of Wefing et al. (2017). Isotope ratios were measured in standard bracketing mode with the Harwell Uraninite standard (HU-1), which is typically diluted to the same signal intensities as the sample. The HU-1 standard is in secular equilibrium and the activity ratios of (^{234}U/^{238}U) and (^{230}Th/^{238}U) being 1. Isotope ratios of samples are used to estimate U-series ages according to the decay equations (Ludwig & Titterington, 1994) calculating with the half-life values for ^{234}U and ^{230}Th published by Cheng et al. (2000).

U-series disequilibrium dating relies on two presumptions: (a) a closed system: no gain or loss other than the decay of the parent nuclide or daughter products since the time of formation, and (b) intermediate and daughter decay products are absent at the time of formation, or can be corrected for. The second assumption, in particular with respect to ^{230}Th, is often not completely fulfilled. All measured samples showed ^{230}Th/^{232}Th activity ratios less than 25 and were all corrected for detrital Th. For the Th correction, a bulk Earth ^{232}Th/^{238}U weight ratio of 3.8 ± 1.9 for detritus is assumed and ^{234}U, ^{238}U and ^{230}Th in the detrital phase in secular equilibrium.

Existing data points from previous studies were used to complement the U/Th dating and, in combination with the log description, petrography and mineralogy, to address the history of travertine deposition and roughly estimate the timing of aragonite to calcite neomorphism. Given the small sample volumes, only four travertine samples that preserved their sedimentary macrofabric were selected for U/Th dating. In addition, two recent samples were analysed to provide a control on the minimum age.

4 | RESULTS

4.1 | Core description and spring carbonate facies

The core can be subdivided into two main parts (Figure 4). The lower part, from 111.8 to 51.7 m (370.0 to 169'0.9 ft), consists of carbonate and siliciclastic sediments. The upper part, above 51.7 m, consists of continuous (spring) carbonate deposits. Emphasis in this study is on the upper part but the description of the lower part is included to frame the context and timing of travertine deposition at MHS.

4.1.1 | Core section: 112.8 to 51.7 m (370 to 169.9 ft)

The bottom 1.2 m are composed of dark to pale grey, finely laminated silty sandstone to mudstone (112.8 to 111.6 m, Figure 4), characterised by poor recovery. Clayey layers and oxidation patches are seen between 112 and 111.5 m depth. From 111.6 m upwards, grey, poor to wavy laminated sandstone appears. Its colour becomes increasingly dark from 104.5 m upwards and the grain size decreases. Following a matrix-supported to clast-supported, carbonate-cemented breccia layer at 101.8 m depth and a recovery gap, the sediments consist of dark, grey-brown, finely laminated to well-bedded siltstones to sandstones. Dark grey, floating clasts at 96 and 93 m depth evolve again into poorly to well-bedded light grey sandstone. At 90.5 m, it changes abruptly into a thin layer of floating clasts of finely laminated sediments, followed by dark grey, coarse sandstone with oxidation patches, alternating with conglomerates with subrounded to subangular fragments (1–10 cm diameter). When compared to the descriptions of geological units in the region by Bargar (1978), the deposits from 112.8 to 89.3 m potentially could be linked to deposits of Permian age.

Between 89.3 and 77.1 m, recovery is poor with fragments of red-green clays, grey sediments and a piece of travertine clast (at 86.2 m). It is unclear whether these strata are in situ or not. At 79.1 m depth, a 0.6 m interval of white, compact carbonate is present. It is covered by a fine

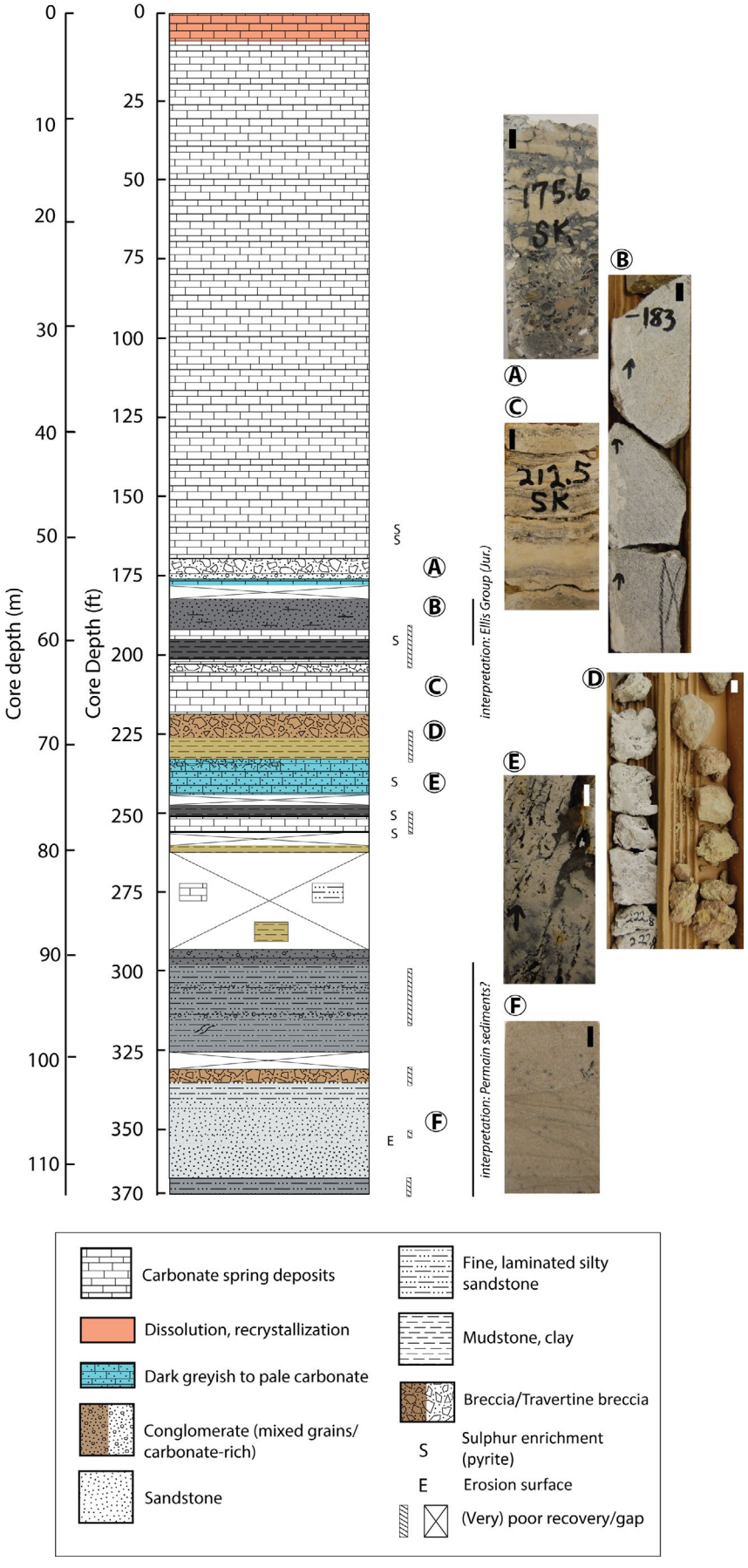

FIGURE 4 Core log of the entire Y-10 core. Photograph insets show core surfaces of different lithologies in the lower part of the core (below 51.7 m/169.9 ft depth). All scale bars are 1 cm. (A) Conglomerate layer overlain by travertine breccia with blackish sediment infill; (B) Carbonate-cemented, grey, coarse sandstone deposits; (C) First occurrence of layered carbonate; (D) Light grey breccia (angular clay clasts in a carbonate matrix), grading into green clay; deposits with (recrystallized) spring fabrics; (E) Dark grey carbonate with high-angle fractures lined by pyrite; (F) Pale grey laminated sandstone with cross lamination

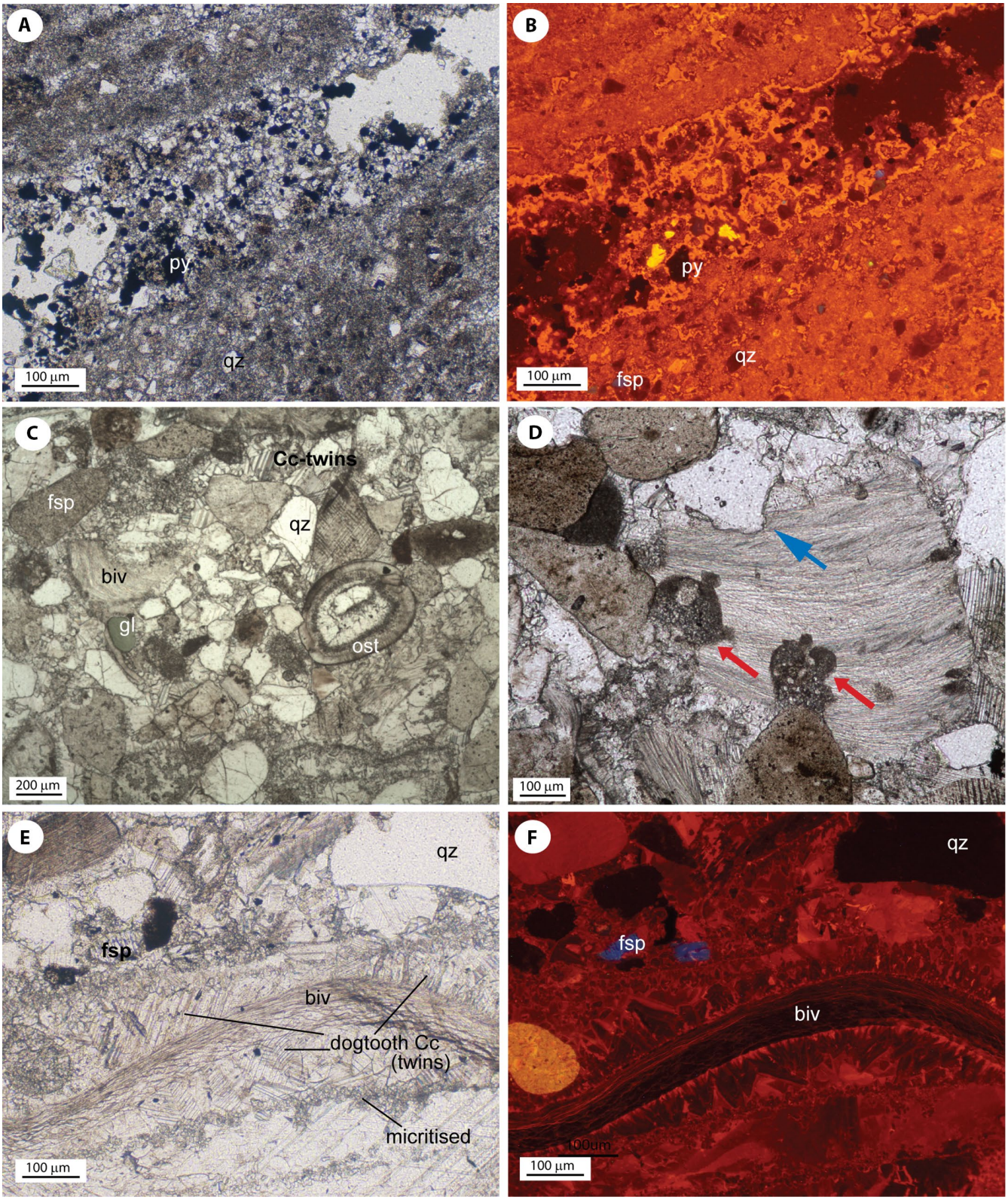

FIGURE 5 Photomicrographs of limestone (A, B) and sandstone (C-F) intervals in lower core section. (A) Micritic limestone with silt-sized quartz and feldspar grains. Fractures are filled with coarser calcite cements and pyrite (py). (B) Cold cathodoluminescence image of (A) showing orange bright to dull luminescent calcite. Fsp = feldspar (blue luminescent), qz = quartz (non-luminescent, black grains). (C) Marine carbonate-cemented (Cc) sandstone with quartz (qz), feldspar (fsp) and glauconite (gl) grains, ostracods (ost) and bivalves (biv). (D) Micrite and sediment filled boring in bivalve fragment (red arrows). Quartz grain is pushed in the shell due to compaction (blue arrow). (E) Micritization of shell fragments and dogtooth calcite cement (Cc) around a bivalve fragment (biv). Grains consist of quartz (qz) and feldspar (fsp). (F) Cold cathodoluminescence image of (E)

black sediment layer that smells of H_2S. Following again a gap, dark greyish to pale micritic carbonate sediments appear at 74.7 m (Figure 4). They show faint sub-horizontal layering and high-angle fractures and vugs that are lined with pyrite. In thin section, dispersed fine siliciclastic quartz and feldspar grains are observed (Figure 5A,B). They have formerly been interpreted as travertine deposits (Chafetz & Guidry, 2003; Sturchio, 1990), but do not resemble spring deposits in thin section. At the top, the micritic carbonates show a breccia of angular clay clasts in a carbonate matrix that grade into red to green clays with poor recovery at 71 m depth (Figure 4). Between 68.9 and 67.3 m, a pale, white to grey breccia is again present with fine-grained clasts floating in a white, carbonate-cemented matrix (Figure 4).

At 67.3 m depth, the first occurrence of carbonate deposits with typical spring fabrics is documented (Figure 4). The interval consists of white, well-layered deposits. Until 63.7 m depth, layering is sub-horizontal, showing vuggy and fenestral porosity. Dendrite features are recognised. At 63.4 m, a fabric resembling coated bubble boundstone (Della Porta et al., 2017) or 'foam rock' (Falk et al., 2016; Gandin & Capezzuoli, 2014; Guo & Riding, 1998) occurs, followed by steeply dipping crystal fan dendrites at 63.1 m depth. These dendrites are covered by brecciated travertine and the section ends with horizontal, well-laminated deposits with branching dendritic textures.

The spring carbonates are covered with dark grey, clayey sediments, interrupted by a thin carbonate bed and then covered by carbonate-cemented, grey, fine to coarse sandstones and conglomerates (Figure 4). The siliciclastic fraction consists of monocrystalline and polycrystalline quartz, feldspars and lithic fragments (Figure 5C,D). Rounded green to brownish glauconite is common (Figure 5C). Marine bioclasts consist of bio-eroded bivalve shells and echinoderm debris (Figure 5C–E). Some shells are strongly micritized (Figure 5E) and circumgranular fibrous to columnar cements can be recognised (Figure 5E,F). Larger, pore filling, anhedral equant calcite cements show cleavage twinning (Figure 5C,E). Macroscopic and microscopic observations indicate that these are shallow marine deposits and they are interpreted as deposits of the Jurassic Ellis Group (Swift Formation; Bargar, 1978; Ruppel, 1982).

Following a recovery gap until 53.9 m, a thin layer of compact, white limestone occurs with greyish streaks, followed by a thin conglomerate layer and a thicker travertine breccia package with black sediment infill and carbonate-cemented vuggy pores (Figure 4). The conglomerate deposits with clayey infill recall diamictite-type deposits observed in the broader Yellowstone and Gardiner area. Around 51.7 m depth, well-bedded to poorly bedded carbonate deposits are present and mark the onset of the continuous carbonate spring succession in the core.

4.1.2 | Core section: 51.7 m (169.9 ft) to surface: Travertine facies and fabrics

Figure 6 shows a more detailed log of the upper travertine section. The interpretation of travertine facies is indicated along the vertical log axis, based on Fouke et al. (2000) and De Boever et al. (2017b) including a distinction between Pond (slope) Facies and Extended Pond Facies in fossil deposits.

The lower 7.3 m consist (51.7–44.5 m) of sub-horizontal, well-laminated deposits with granular and crust fabrics (Extended Pond Facies; De Boever et al., 2017b). Porosity consists of bedding-parallel fenestral and partly cemented vuggy porosity. At 46.3 and 43.9 m, intraclasts occur. At 42 m depth, spherules (Fouke, 2011), suggesting a Distal Slope Facies deposits, appear for the first time. They are subrounded and can reach 4 mm in diameter. They occur in beds between the sub-horizontal, well-laminated deposits. Spherules (Della Porta, 2015; Fouke, 2011) may possess a core consisting of a micritic clast, but often a clear core structure is missing (Figure 3D). The core is surrounded by radial oriented, compact, branching dendrites. Occasionally, dendrites grow longer along one side of the spherules, in a direction perpendicular to the bedding. Other microfabrics consist of poorly to strongly branching dendrites and a micritic to peloidal texture (Figure 3E).

At 40.2 m depth, fabrics that resemble 'calcite rafts' (Gandin & Capezzuoli, 2014; Pentecost, 2005) are present. They consist of flat lying, elongated $CaCO_3$ chips, encrusted by a fine, whitish cement at the top and bottom. They might belong to the cored top of Distal Slope sediments, or rather reflect a Pond Slope Facies. They are overlain by dipping laminae of dendritic crusts (Proximal Slope Facies), followed by well-laminated, but vuggy, sub-horizontal layers. Streamer fabrics (Apron-Channel Facies) appear for the first time at 36.3 m depth. They are characterised by faint laminae and millimetre-wide to centimetre-wide, elongated pores that drape underlying deposits (Figure 6). Core recovery in the Apron-Channel Facies is poor and large, partly cemented vugs are common.

Above 32.0 m depth, a sub-horizontal, laminated alternation of fine, granular and crust fabrics dominate (Figure 6). Laminae are crinkly or undulating. They may bifurcate and merge again. Millimetre-sized, layer parallel pores enhance the laminated appearance (Pond Slope Facies). At 28.0 m, the slope of the travertine beds increases. These Proximal Slope Facies deposits are dominated by elongated dendritic or more shrub-like crusts. Microscopically, they show diverse textures (Figure 3F). In terms of morphology (Della Porta, 2015), they could be described as: (a) dark-light laminated, or brown-greyish crystals or crystalline fans, (b) poorly branching dendrites and (c) millimetres to centimetres long, branching dendrites. Crystal fans are composed of subparallel to fanning-out columnar crystals with wavy extinction.

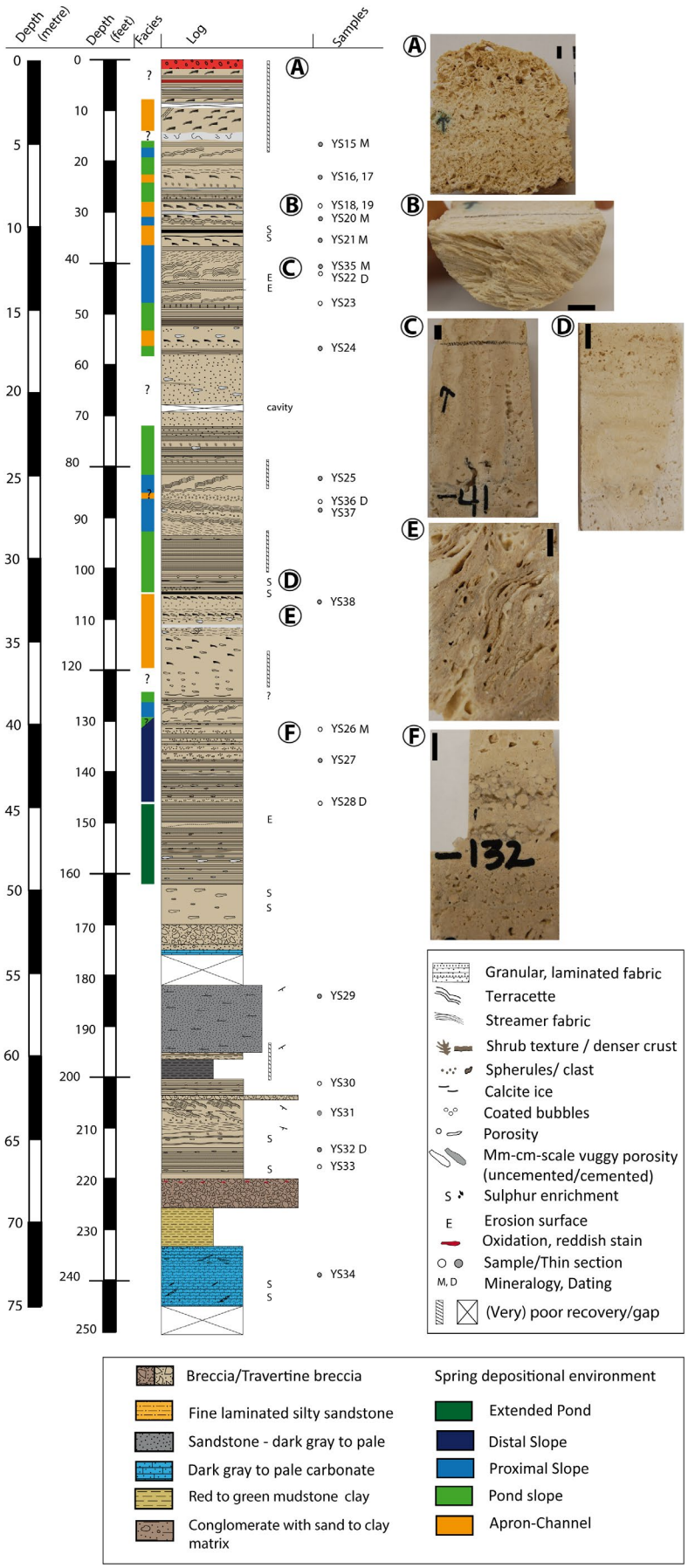

FIGURE 6 Detailed log of the Y-10 core section above 245 ft (74.5 m). Interpretation of travertine facies following Fouke et al., (2000) and De Boever et al., (2017b) is given together with sample locations. Photograph insets show details of different travertine facies and fabrics. All scale bars are 1 cm. (A) Strongly indurated fabric with secondary porosity at the top of the core. Lamination can only be discerned in places. Arrow points to the top; (B) Streamer deposits that resulted from carbonate encrusting microbial filaments; (C) Nearly vertical laminae of dendritic crusts; (D) Fine laminae of granular and crust fabrics; (E) Streamer fabric characterised by millimetre to centimetre-wide, elongated pores that drape underlying deposits; (F) Spherulite and a laminae with fine, granular and crust fabrics

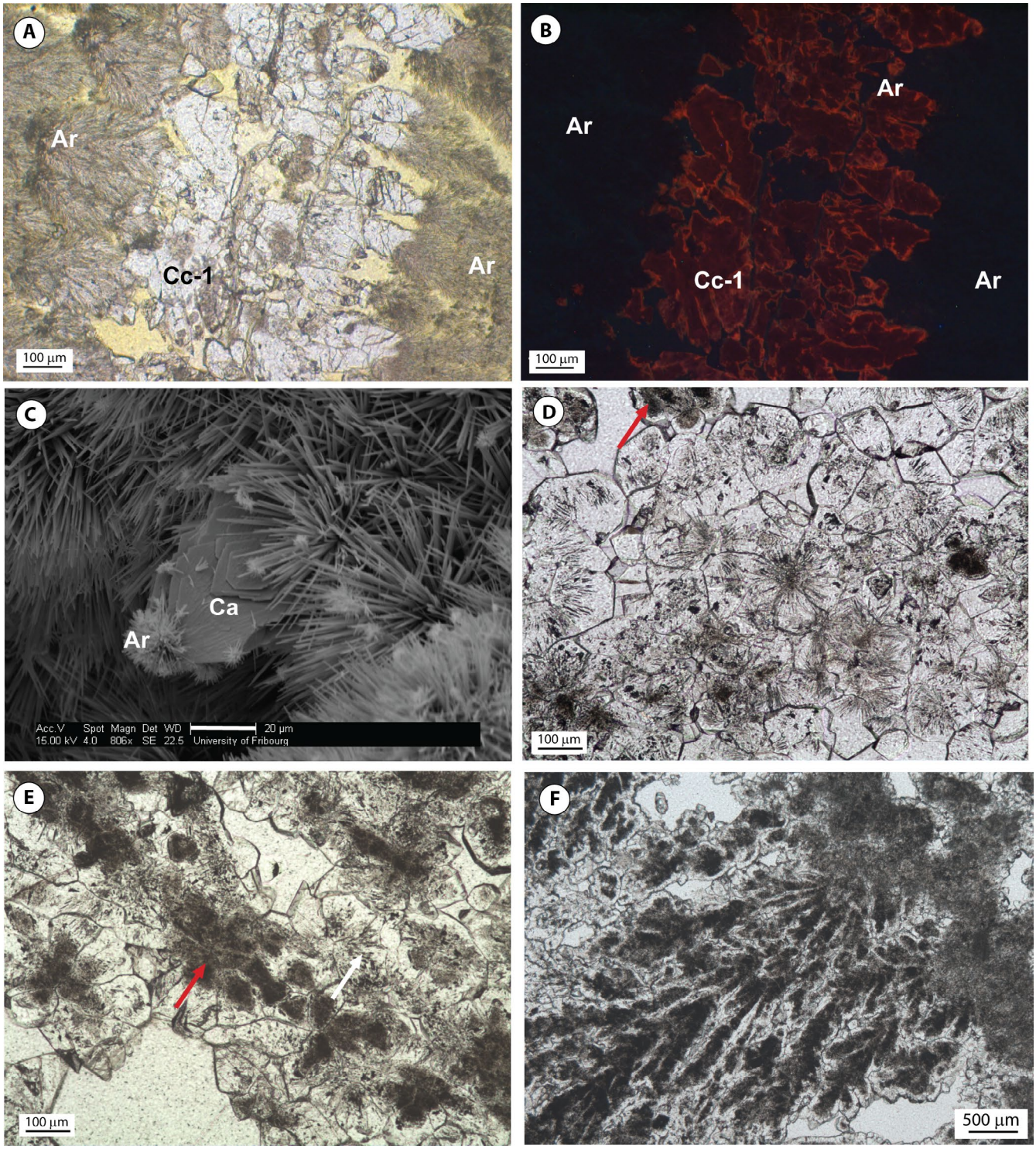

FIGURE 7 Photomicrographs of travertine deposits. (A) Transmitted light image of calcite Cc-1 cementing and overgrowing aragonite (Ar) in a Proximal Slope sample at Narrow Gauge spring. (B) Cold cathodoluminescence image of (A) showing that only the calcite shows up as dull orange luminescent. (C) Detail of aragonite needles in Pond Slope deposits that are overgrown by a calcite crystal (Ca), which is, in turn, the seeding point for a bush of outwardly radiating aragonite needles (Ar). (D) Aragonite needle ghosts radiate outwards, similar to their modern counterparts in the Apron-Channel facies. They are here engulfed and enclosed within calcite cement. In some places, only a brownish, cloudy core can be seen within the calcite crystals and no needle pseudomorphs remain (red arrow; Y-10, sample 21). (E) Zoom out: Alignment of outwardly radiating aragonite needle ghosts (white arrow), similar to modern streamer deposits. Another part of the image (red arrow) shows aligned, brownish, cloudy crystals that are surrounded by transparent calcite cement. No needle pseudomorphs can be seen (Y-10, sample 21). (F) Dendritic textures with greyish cloudy crystal core and transparent calcite crystal rim (Y-10, sample 27)

Internally, crystals display alternating very dark to lighter brownish laminae. Within such dendritic texture, laminae can be followed over different crystals.

At 26.8 m depth, fabrics that vaguely resemble streamer deposits are observed and interpreted as a potential short shift to Apron-Channel Facies. The slope direction then changes and the beds flatten out, marking a transition to sub-horizontal, laminated deposits. From 21.9 to 16.1 m depth, the carbonate spring macrofabrics become more uniform, resulting in a white, porous limestone with millimetre-sized round to elongated, aligned pores which become partly cemented upwards. Around 15.8 m, white, sub-horizontal crust layers appear again. They are overlain by gentle to steeply sloping Proximal Slope Facies crusts with microterracette morphologies (9.7 m) that alternate with streamer fabrics of the Apron-Channel Facies (Figure 6).

Towards the top of the core, it becomes difficult to recognise distinct depositional facies. Above 8.5 m, sub-horizontal laminae with shrubs suggest a Pond Slope Facies. Overlying, sloping crusts indicate a Proximal Slope Facies. From 4.5 m up, small-scale chaotic layers with slopes in different directions, well-cemented secondary cavities and recrystallized streamer deposits (Apron-Channel Facies) are covered by nearly vertical crusts. The top 2.1 m of the core is dominated by dissolution cavities (Figure 6), orange-brown colouration and uniform, white calcium carbonate.

4.2 | Microscopy of diagenetic phases

Whereas the travertine macrofabrics are identifiable within the core and can mostly be linked to modern depositional facies at MHS, their microscopic textures are often modified. In the following, the observed diagenetic phases and events are described and illustrated.

4.2.1 | Aragonite neomorphism, calcite overgrowth and cementation (Cc-1)

In modern samples, stacked aragonitic shrubs are interlaid by a 100–200 μm thick lamina of clear calcite crystals. In a Proximal Slope sample, calcite crystals (henceforth called Cc-1), which partly replace aragonitic shrub crystal aggregates, stand out in CCL because of their dull orange colour that contrasts with the non-luminescent aragonitic shrubs (Figure 7A,B). In a sample from a modern Pond that was dry at the moment of sampling (Figure 2D), calcite rhombs overgrow the aragonite needles both in the core of individual granular fabrics as well as along the rim. In places, radial growing aragonite needle bushes nucleate again on top of these calcite rhombs (Figure 7C), suggesting that precipitation and equilibrium conditions for the $CaCO_3$ polymorphs changed regularly over time.

Within the Y-10 core, fine, tens of microns long, needle-like ghosts can still be observed in the core of granular to equant and elongated calcite crystals (Cc-1, Figure 7D), recalling the shape of shrubs, spherules or fans. They recall the aragonite needle crystal textures typical of the modern deposits. Several of the needle pseudomorphs are engulfed or overgrown by a single calcite crystal. In a further stage, when the needle morphology becomes faded, as is the case for most of the fabrics in the Y-10 core, only dark, brown-greyish calcite crystals remain. Depending on the primary fabric, they are organised in fan or branching dendritic textures (Figure 7E,F). The SEM shows that these crystals inherit their cloudiness from a high density of micron-sized pores, ranging in size from 1 to 10 μm (Figure 8A). The surrounding clear crystal rim often grows in optical continuity with the cloudy crystal core. The Cc-1 calcite crystals typically have a mottled dull to bright orange luminescence in their porosity-rich core, overgrown by brownish-orange dull luminescent zones in the rim (Figure 8B,C). When Cc-1 crystals are elongated, alternations of more porous, denser zones become apparent.

4.2.2 | Dissolution and micrite cement (Mc-1)

The outline of textures, such as dendrites, spherules and Cc-1 cements, is, in places, irregular or 'smoothed'. It points to a local dissolution phase. The primary interparticle and framework porosity and the secondary vuggy porosity may also be lined by a single, thin or composite, 100 μm thick, micritic band (Mc-1; Figure 8D,E). Although rarely observed, the micritic band(s) cover different, sometimes opposite (lower and upper) sides of vugs and bridge pore spaces between different spherules. An origin related merely to the infiltration of fine $CaCO_3$ sediment can, in this case, be excluded. The Mc-1 phase is crinkled and discontinuous and displays a dull orange luminescence.

4.2.3 | Equant to elongated calcite cement (Cc-2)

Subhedral, equant calcite crystals or a rim of elongated to columnar calcite crystals (henceforth called Cc-2) partly fill framework or vuggy porosity, throughout the core (Figure 8D,E). Towards the centre of millimetre-sized pores, Cc-2 crystals become equant and may give rise to a tight mosaic. When Mc-1 is absent, they seed directly on Cc-1 crystals. In the latter case, both phases are difficult to distinguish given their similar luminescence characteristics. Cc-2 crystals growing on Mc-1 may be darker and cloudy with inclusions that display a bright orange luminescence yielding an overall blotchy luminescence.

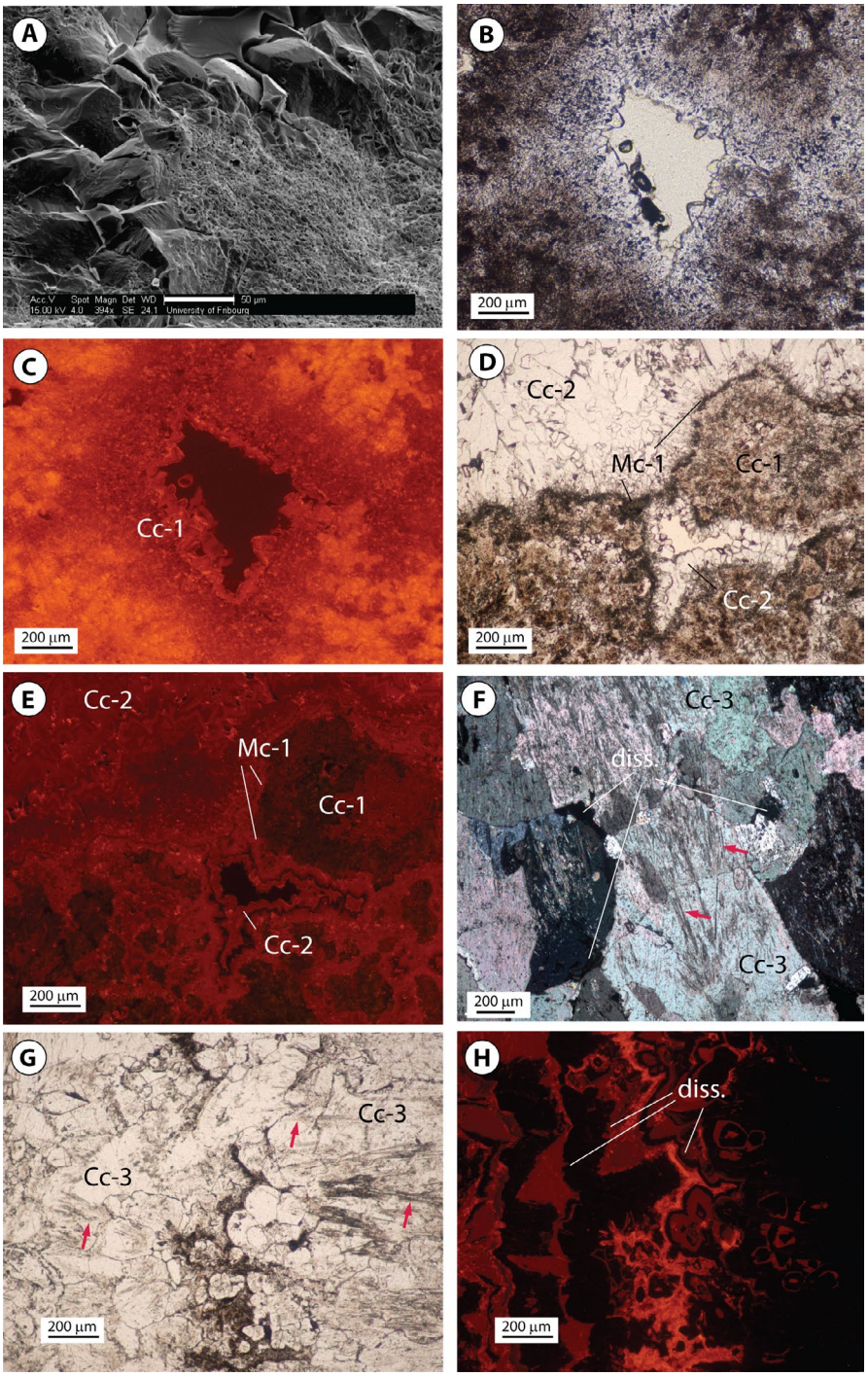

FIGURE 8 Photomicrographs of travertine deposits (TL = Transmitted light; CCL = Cold cathodoluminescence). (A) SEM-SE image of cloudy calcite crystal core that is microporous and a rim of dense calcite crystals, lacking microporosity (Y-10, sample 27). (B) Zoom of rim of spherule consisting of cloudy, grey-brownish crystals and a rim of Cc-1 cement that gradually becomes more transparent towards the pore centre (Y-10, sample 27). (C) CCL of B showing the bright yellow-orange spherule and dull orange Cc-1 cement rim which has a blotchy appearance where the crystal is cloudy in transmitted light and finely zoned when it is transparent. (D) TL image of irregular spherules, surrounded by a micritic rim that connects and bridges between them, followed by a Cc-2 cement phase (Y-10, sample 38). (E) CCL image of (D) showing the irregular outline of the spherule and heterogeneous texture within, possibly related to neomorphism and Cc-1 overgrowth, cementation. (F) Needle textures in large Cc-3 mosaics becoming particularly clear under polarized light (red arrows). Different groups of needles are enclosed in one calcite crystal. The Cc-3 crystals further show dissolution vugs (diss.; Y-10, sample 15). (G, H) TL and CCL image, respectively, of coarsely laminated travertine that is heavily recrystallized and cemented: Cc3-cements with needle pseudomorphs (red arrows). Cathodoluminescence reveals numerous dissolution surfaces in the Cc-3 crystals pointing to alternating cementation and dissolution during formation (Y-10, sample 15)

TABLE 1 Quantitative results of Rietveld analysis of XRD data for recent samples from Narrow Gauge spring and the Y-10 core

Sample	Depth (m)	Facies	Calcite %	Mg%	Aragonite %	Gypsum %	GOF
Narrow Gauge							
YS01	Surface	Proximal Slope	5.4	4.1	93.0	1.6	2.2
YS02	Surface	Proximal Slope	7.8	3.9	89.1	3.0	1.9
YS04	Surface	Apron-Channel	1.3	1.3	98.7		2.5
YS06	Surface	Proximal Slope—Pond Slope	5.7	4.0	94.3		2.0
YS14	Surface	Proximal Slope	3.6	1.3	96.4		2.3
YS39	Surface	Pond Slope	5.2	3.0	94.8		2.0
YS45	Surface	Proximal to Distal Slope	41.9	2.7	58.1		2.9
YS50	Surface	Distal Slope	7.8	1.5	92.2		2.7
Y-10 core							
YS15	5.1	Pond Slope?	95.5	0	4.5		7.4
YS20	9.7	Proximal Slope	99.5	0	0.5		6.6
YS21	10.8	Apron-Channel	99.6	0	0.4		3.0
YS35	12.4	Proximal Slope	100.0	0.9			3.5
YS22	12.7	Proximal Slope	100.0	0			2.9
YS36	26.5	Proximal Slope	100.0	0.7			2.5
YS26	40.2	Distal Slope	100.0	0.8			3.6
YS28	44.4	Extended Pond/Distal Slope	100.0	0			2.4
YS31	63.2	Proximal Slope	100.0	0.2			4.0
YS32	65.4	Pond Slope?	100.0	0.6			2.6
YS33	66.6	Pond Slope?	100.0	0.2			4.3

Mg% represents the estimated Mg content within the calcite phase.

Abbreviation: GOF, goodness of fit.

Subsequently, more transparent zones show a fine, dull to orange-zoned luminescence and occasionally a first non-luminescent zone (Figure 8E).

4.2.4 | Dissolution and columnar to elongated and poikilotopic calcite (Cc-3)

Near the top of the core, equant to columnar and poikilotopic calcite crystals (up to 1 mm across), henceforth called Cc-3, occur (Figure 8F). They were not observed further down the core. Their luminescence shows a complex sequence of dark dull and non-luminescent zones, which are, in places, orange speckled. These zones are often discontinuous, showing numerous pits and clear phases of dissolution in between (Figure 8G,H). In the porous sequences at the very top of the core, Cc-3 forms transparent calcite cement rims around aragonite needle relics or ghosts (Figure 8F). In some cases, ghost and relic textures can be traced continuously over different calcite crystals. Elsewhere, the needles form laminae within one single poikilotopic calcite crystal. The aragonite ghosts and relics enclosed in Cc-3 crystals yield a blotchy bright orange luminescence.

4.2.5 | Late dissolution

A last dissolution phase results in smoothed crystal outer surfaces, dissolution pits and secondary intracrystalline porosity (Figure 8F). The cloudy zones in the core of Cc-1 crystals, where aragonite relics might have been present, are primarily attacked by this dissolution phase leaving the transparent crystal rims more intact. Dissolution vugs and crystal rims affected by dissolution are most commonly observed in the top 6 m of the core, but also at greater depths, around 24 m and 33.5–36.6 m.

4.3 | Mineralogy

The mineralogy of travertine samples is given in Table 1. In Recent samples from the surface of Narrow Gauge and New Grassy Springs, aragonite shows concentrations above 90% except for one sample at the Proximal to Distal Slope with 58% aragonite. In contrast to the surface samples, in the core samples, calcite is the dominant phase between depths of 5–40 m. Aragonite has only been encountered in the first 10 m of core and its concentration drops rapidly to <1%

below 5 m (Figure 9). Based on lattice parameters of calcite (*a* lattice parameter; Titschack et al., 2011), the Mg content of the calcite mineral can be estimated. All samples have concentrations below 5%. The modern samples have slightly higher concentrations (1.3%–4.1%) compared to those of the Y-10 core (≤1% Mg).

4.4 | Stable carbon and oxygen isotopes

4.4.1 | Bulk samples

Travertine deposits, other limestone units and carbonate-cemented horizons from the core were examined for their bulk stable isotopic signature (Figure 10A). The data are compared with results of solid, modern travertine precipitates published by Fouke et al. (2000) for springs at Angel Terrace and other modern deposits at Narrow Gauge and New Grassy Spring (Table S1). The isotopes of the continuous travertine sequence (above 51.8 m) show a positive trend of $\delta^{13}C$ (2.6–4.8‰ V-PDB) and $\delta^{18}O_{VPDB}$ (−27.3 to −21.2‰ V-PDB). The positive $\delta^{13}C$–$\delta^{18}O_{VPDB}$ trend for the Y-10 core travertine is shifted by around 2‰ to slightly heavier carbon isotope values than for sub-Recent travertine from two active springs (Narrow Gauge and Angel Terrace; Fouke et al., 2000), but the cloud of sample values does overlap.

However, a very clear, upstream to downstream trend with facies, as observed in Recent travertine deposits, is lacking for the core (Figure 10A). The vertical trend along the core length shows that between the bottom of the continuous travertine section, at 51.8, and 8.8 m depth, $\delta^{13}C$ values vary from 4.5 to 2.6‰ (Figure 10B). The $\delta^{18}O_{VPDB}$ values vary between −23.0 and −26.0‰. Values at the very top of the core show $\delta^{18}O_{VPDB}$ values down to −27.1‰ and lower $\delta^{13}C$ values (down to 1.6‰).

In the lower core section, travertine deposits underlying marine sandstones plot within the same $\delta^{13}C$–$\delta^{18}O_{VPDB}$ travertine trend towards the most positive end. Two samples from carbonaceous sandstones that occur between the travertine of the upper core section and those in the lower section (Figure 4) have similar isotopic signatures with a $\delta^{13}C$ value around 1.5‰ and $\delta^{18}O_{VPDB}$ around −13.5‰ (Figure 10A). A single measurement for the micritic-silty limestone at 72.8 m depth plots also within the cluster of travertine samples.

4.4.2 | Spot analyses

The bulk analyses are complemented with spot analyses using micro-SIMS to investigate if the diagenetic and fluid history could be further detangled (Table S2). Cc-1 calcite overgrowing aragonitic shrubs and forming a continuous lamina in a Recent sample of Narrow Gauge Spring show large variation in $\delta^{13}C$ values (mostly between −2.2 and 3.3‰) and less variation in $\delta^{18}O_{VPDB}$ (−30.0 to −29.7‰). Values are 0.8–6‰ and 4.5–5.2‰ lower for carbon and oxygen, respectively, compared to the bulk value (Figure 11A–C).

Similarly, in the Y-10 core, some zones of transformed, dendrite or spherule textures, that are now microsparitic, have a range of $\delta^{13}C$ signatures lower than the $\delta^{13}C$ bulk value (Figure 11D–F). The $\delta^{18}O_{VPDB}$ values are similar to or lower than the bulk signature. Blotchy dull luminescent to transparent and zoned dull luminescent Cc-1 calcite possesses $\delta^{13}C$ values within the range of or slightly below the bulk values,

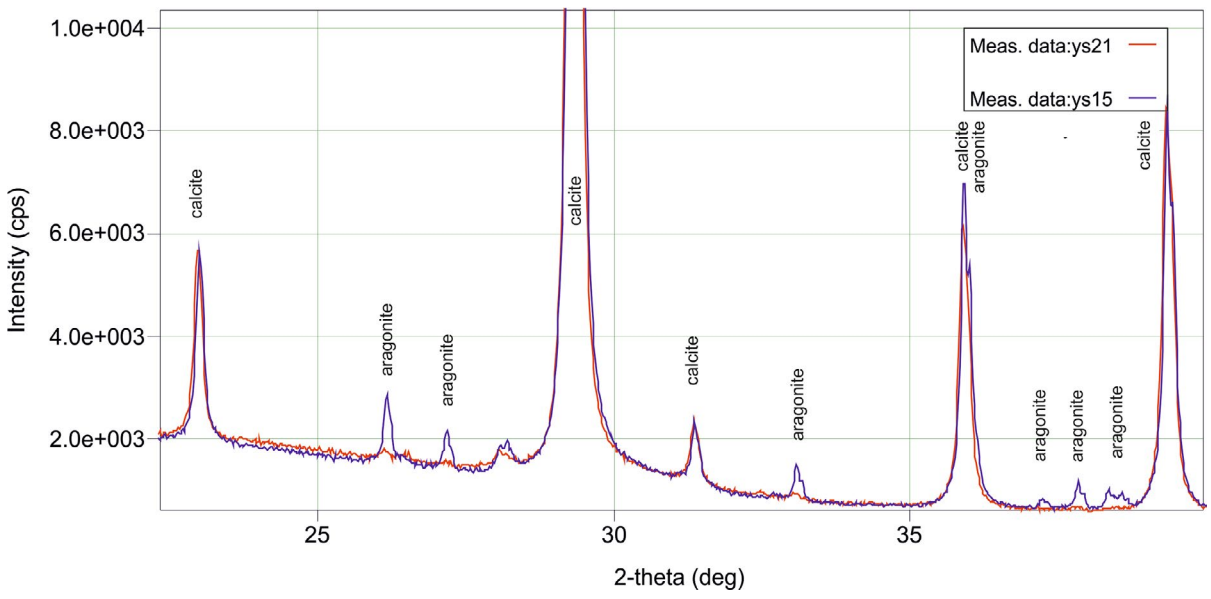

FIGURE 9 Comparison of XRD spectra between 22.5 and 40° 2Θ of Y-10 core samples 15 (5.1 m) and 21 (10.8 m). Aragonite peaks can be seen and quantified in sample 15, but are poorly defined in sample 21 making quantification difficult (<1%). cps, counts per seconds; deg, degrees

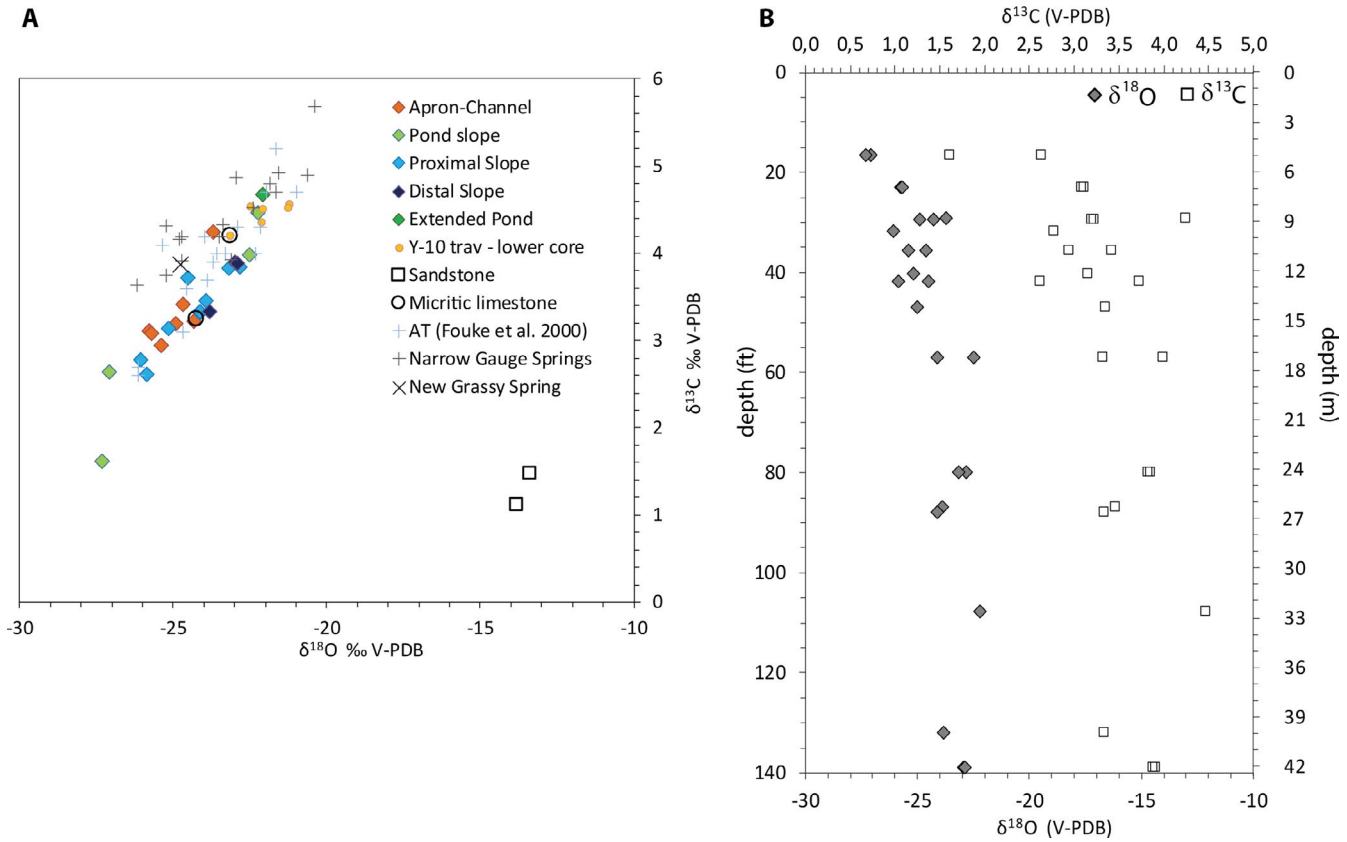

FIGURE 10 Bulk stable carbon and oxygen isotope results. (A) $\delta^{13}C$–$\delta^{18}O_{VPDB}$ cross-plot of data from the Narrow Gauge springs and the Y-10 core together with data of the MHS system as reported by Fouke et al. (2000). AT, Angel Terrace. (B) $\delta^{13}C$ and $\delta^{18}O_{VPDB}$ data of all travertine samples with depth in the top 42.6 m (140 ft) of the core

and $\delta^{18}O_{VPDB}$ values are dominantly lower than the results obtained from bulk samples (Figure 11D–I). While $\delta^{13}C$ tends to be higher than values measured in the cloudy crystals building composite textures, the $\delta^{18}O_{VPDB}$ values possess lower values.

The Mc-1 phase has a variable $\delta^{13}C$ and $\delta^{18}O_{VPDB}$ signature (Figure 11G–I). Both carbon and oxygen isotopes show values below the bulk sample value. $\delta^{13}C$, in particular, shows a negative shift to values as low as −1.74‰, lower than any of the primary structures. Cc-2 crystals possess $\delta^{13}C$ and $\delta^{18}O_{VPDB}$ values slightly lower, around 2–1.6‰, respectively, than the bulk value (Figure 11G–I). A columnar to poikilotopic calcite Cc-3 cement with dull non-luminescent zones shows $\delta^{18}O_{PDB}$ values around and mostly above the bulk value with a shift of 1.5‰ (Figure 11J–L). The $\delta^{13}C$ values show an even larger variation of up to 8.2‰ (Figure 11J–L). Although the number of analysed spots of Cc-3 is limited, the crystals seem to possess a broader range in $\delta^{13}C$ isotopic signature and slightly higher $\delta^{18}O_{VPDB}$ values. This could be in agreement with an inverted J-trend for this cement generation. Such a trend is often found in meteoric (altered) carbonates and characterised by invariant oxygen isotope values coupled with variable carbon isotopic values (Lohmann, 1988; Moore & Wade, 2013). This is in accordance with the faint trend of bulk values towards the top of the core (Figure 10B).

In two samples, an attempt was made to compare the signature of aragonite needle pseudomorphs and the surrounding calcite cement rim (Table 2). Analyses were rarely successful due to spot size and micron-scale topography resulting in erroneous measurements.

4.5 | Dating

Sturchio (1990) and Sturchio et al. (1994) used Th/U dating and radiogenic ^{226}Ra isotopes as part of a broader study in the Yellowstone-Gardiner region (Table 3). Their samples consist of travertine from the very porous top of the core (at 0.7 m depth) and one core sample below the base of the continuous travertine section (at 72.9 m depth). The latter does not show macroscopic or microscopic features typical of spring deposits (Figure 6). To shed further light on the history of spring carbonate deposition and diagenesis, it was therefore decided to revisit the dating of spring carbonates in the Y-10 ($n = 4$) with reference to surface samples of Recent travertine at Narrow Gauge Spring ($n = 2$). The results are summarised in Table 3. The uranium concentrations are low and range

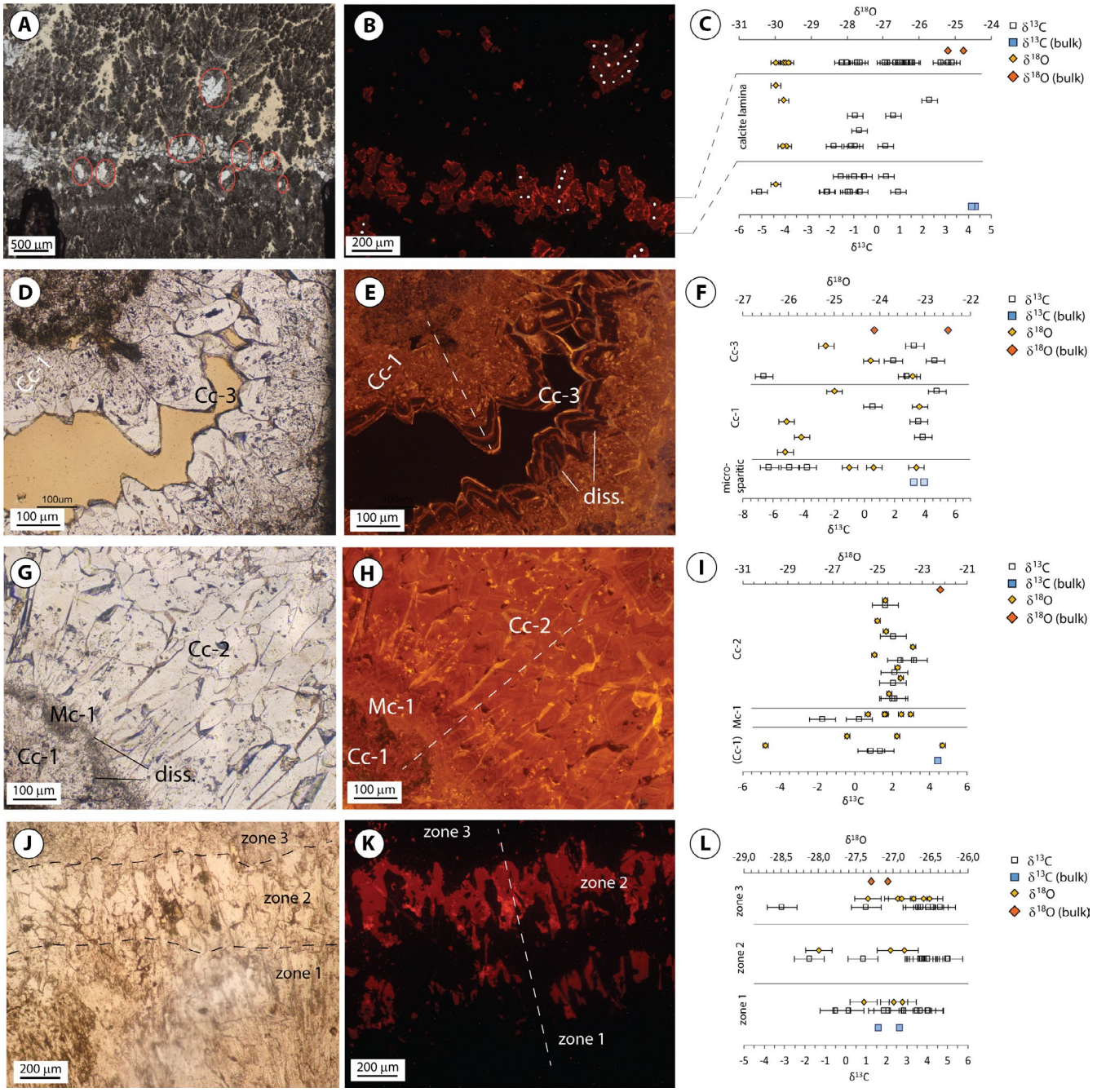

FIGURE 11 Location and results of isotope spot analysis using SIMS. For each sample is given: one transmitted light image and one cold cathodoluminescence light image of the transect analysed (dashed lines) and results of individual spots versus the bulk isotope values of the sample. Error bars indicate one standard deviation. For cement abbreviations: see text. Diss. = dissolution. (A–C) Narrow Gauge spring sample (01). Calcite crystals above and below the Cc-1 lamina replace aragonite. Image in A reflects the total chip used for micro-SIMS and all crystals analysed are encircled in red. The image in B is a zoom of A with individual spots marked. Each horizontal line in the isotope plot (C) reflects analyses from a different crystal. (D–F) Y-10, sample 24. (G–I) Y-10, sample 38. (J–L) Y-10, sample 15

between 7.338 ± 0.010 and 820.823 ± 0.044 ng/g. The ^{232}Th concentrations are elevated, related to detrital input, which is usual for travertine deposits, but renders the application of U/Th dating difficult. The thorium concentrations and ^{230}Th/^{232}Th activity ratios are particularly variable and generally lower than *ca* 25 for all samples. Hence, relative age corrections due to detrital thorium are sometimes large. The corrected ages (Table 3) are younger than the uncorrected ages by 3%–17%. The surface samples have corrected U/Th ages of 0 and 0.4 ± 0.17 ka. Those samples have corrected ages which are younger by 44% and 100%, respectively.

Sample YS32 is located below the continuous travertine section, at a depth of 65.4 m, under a package of sandstones. It has up to 15- to 100-fold higher uranium concentrations

	Needle shape	Transition	Calcite rim	Analyses
$\delta^{13}C_{av}$ (V-PDB)				
Y-10-15	2.52 ± 0.87	3.60 ± 0.87	4.42 ± 0.87	$n = 25$
Y-10-21	Failed	Failed	Failed	
$\delta^{18}O_{av}$ (V-PDB)				
Y-10-15	−26.22 ± 0.18	—	−26.83 ± 0.18	$n = 6$
Y-10-21	−25.58 ± 0.16	—	−25.44 ± 0.16	$n = 12$

One standard deviation given.

TABLE 2 Comparison of average $\delta^{13}C$ and $\delta^{18}O$ values (V-PDB) in aragonite needle pseudomorphs, discontinuous needle pseudomorphs (transition) and the calcite cement rim around

than the other samples. It should be noted that all samples show a similar $\delta^{34}U_i$ signal of 1,083–1,334‰, except for sample YS28 (706‰). This could suggest another uranium source in the waters from which these first travertine deposits, at the bottom of the continuous travertine section, formed.

Two samples were analysed twice, once as a powder, like all samples, and a second time, starting from a small rock piece allowing more careful cleaning just before dating. For sample YS36, both results are comparable. For sample YS28, with an anomalous $\delta^{34}U_i$ signal, the analyses lead to significantly different results. The ages of the samples near the base of the continuous travertine section (YS28) and the travertine below the sandstones (YS32) have to be interpreted with caution regarding their elevated thorium concentrations and age inconsistencies in duplicate analyses. The lowermost sample of the continuous travertine section (YS28), at 44.3 m depth, is older (*ca* 13.4–17.9 ka) compared to the travertine deposits, at 65.4 m (YS32), dated 6.5 ka, and lying underneath the (Jurassic) marine sandstones of the Ellis Group (Swift Formation). Sturchio (1990) found an age of 7.7 ka for their deepest sample at 72.9 m depth.

5 | INTERPRETATION AND DISCUSSION

5.1 | Palaeo-environmental evolution of travertine deposition in the Y-10 core: Macrofabrics and depositional facies

The Y-10 core fabrics and facies were described, reinterpreted and linked to those of the active springs. As microfabrics remain well preserved, depositional facies are still visible and interpretable in most of the core. The link with fabrics in Recent deposits was particularly straightforward for the Proximal Slope Facies, the Distal Slope and to a lesser extent for the Pond Slope and Apron-Channel Facies. This allowed the vertical succession to be interpreted together with evolution of the spring environments cored at that location, even though the 1D core lacks the 2D-3D lateral complexity as seen in outcrop. The roughly 50 m of continuous travertine deposition in the Y-10 core shows an upward evolution from more distal towards more proximal facies. Spherulitic fabrics are formed which are currently known from the cooler, Distal Slope Facies. Calcite rafts appear, which are characteristic of CO_2-rich, standing waters, and gastropods have been recognised in this part of the core by Chafetz and Guidry (2003). These observations suggest a laterally extensive pond or low-angle apron, fed by hot springs. A similar facies underlies the onset of terraced, travertine mounds in travertine quarries in Denizli (Turkey; Claes et al., 2015) and Italian Pleistocene travertine quarries (Della Porta et al., 2017; Guo & Riding, 1998), where it can be traced over tens to hundreds of metres laterally.

5.2 | The fate of travertine fabrics

The diagenetic history of the spring carbonates in the Y-10 core at MHS provides valuable insight into how travertine is preserved in the geological record. In sub-Recent travertine samples, from Vent to Proximal Slope, aragonite dominates as the primary precipitate at MHS. However, even in these samples, equant, sparry calcite crystals cover and replace laminae with aragonitic textures and may be covered, in turn, by a new phase of aragonitic, composite crystal textures such as shrubs. Based on the appearance of neomorphism and calcite cementation within active springs, it can be concluded that primary precipitation and the onset of diagenesis are virtually coeval at MHS.

The different fabrics and facies throughout the entire travertine section were examined petrographically. The sequence of observed diagenetic events and associated textures are consistent throughout and are not related to initial facies or fabric differences. Neomorphism, overgrowth and cementation tend to create a microscopic texture of interlocking mosaic calcite crystals, with cloudy, microporous crystal cores in which the details of primary lamination and composite crystal texture gradually disappear (Figure 12). In some cases, the rough morphology of the initial texture, that is, shrubs or spherules, can still be discerned, although the mineralogy has changed. Early diagenetic neomorphism and cementation in spring deposits at MHS may thus result in the homogenization of primary features (Figure 12).

TABLE 3 Uranium-thorium (U-Th) ages of surface (Narrow Gauge Spring) and subsurface (Y-10 core) travertine samples presented in this work. For comparison, previous dates by Sturchio (1990) and Sturchio et al. (1994) using α-spectrometry and TIMS have been incorporated in the table. [1]:AR = activity ratios; i: initial. All measurements are performed with MC-ICP-MS, NEPTUNE. All errors are 2σ. All ages are corrected for detrital Th assuming bulk Earth $^{232}Th/^{238}U$ weight ratio of 3.8 ± 1.9 for the detritus and ^{230}Th, ^{234}U and ^{238}U in secular equilibrium

m depth	Sample name	^{238}U (ng/g)		^{232}Th (ng/g)		$(^{230}Th/^{238}U)^{1}$		$(^{230}Th/^{232}Th)^{1}$		$\delta^{234}U$ (‰)		$\delta^{234}U_i$ (‰)		Age (corr.) (ka)		$^{228}Ra/^{226}Ra$ (ka)
0[a]	YS03	25.749	0.019	0.7342	0.0008	0.01555	0.00090	1.687	0.098	1332.6	3.3	1334.1	3.4	0.40	0.17	
0[a]	YS04	17.848	0.015	2.1255	0.0042	0.02627	0.00142	0.681	0.037	1289.3	6.0	1289.3	6.0	0.00		
12.7	YS22	8.223	0.011	0.0843	0.0003	0.08141	0.00356	24.386	1.071	1219.1	7.5	1232.7	7.7	3.95	0.19	
26.5	YS36	7.338	0.010	0.4735	0.0011	0.10137	0.00590	4.832	0.281	1068.9	9.9	1083.0	10.2	4.63	0.57	
26.5	YS36[b]	8.090	0.007	0.2900	0.0010	0.10877	0.00510	9.204	0.432	1107.6	7.5	1124.3	7.7	5.31	0.38	
44.4	YS28	64.380	0.031	11.4456	0.0145	0.23461	0.00220	4.064	0.038	679.7	2.9	706.0	4.2	13.44	1.51	
44.4	YS28[b]	25.501	0.006	2.7370	0.0070	0.27359	0.00389	7.724	0.112	643.0	2.9	676.4	3.6	17.93	0.95	
65.4	YS32	820.823	0.044	20.6085	0.0327	0.13626	0.00046	16.717	0.063	1257.9	1.2	1281.1	1.4	6.46	0.16	
0[a]	Narrow Gauge[c]	15.75	0.03											<0,001		
0.7	Y10-2.4 ft[d]															≤0.037
72.9	Y10-239.3[d]	1.85	0.09											7.7	0.4	

[a] Surface samples from Narrow Gauge spring.

[b] Sample dated second time, starting from a sample piece.

[c] Sturchio et al. (1994).

[d] Sturchio (1990).

A comparison of Y-10 core samples with the modern deposits has shown that neomorphism, that is, the polymorphic transformation of aragonite to calcite, is one of the first and most pervasive, early diagenetic processes. Two types of microscopic textures can be distinguished:

1. Calcite mosaics enclosing relics of aragonite needles. The fibres can be followed across different calcite crystals or several of them are engulfed by a single calcite crystal (Cc-1 or Cc-2; Figure 12). Finally, they become discontinuous, isolated patches in the calcite crystal (Figure 12). The XRD analyses demonstrated that in places, these fibres are not only textural ghosts, but also aragonite relics that preserved their mineralogy. At depths between 5 and 10 m, aragonite decreases below 1%, although ghost textures can still be observed. Similar features have been described from speleothem deposits (Martín-García et al., 2009, 2014; Martín-Pérez et al., 2012) and non-marine cool or hot springs (Arp et al., 2001; Golubić et al., 2008).
2. Microtextures consisting of a microporous, microcrystalline crystal core with a brown, cloudy appearance in transmitted light, surrounded by a transparent, dense calcite rim (Figure 12). The second texture is often observed adjacent to the first, but is more widespread in the Y-10 core samples studied.

The process of aragonite to calcite neomorphism has been found to involve microscale dissolution of metastable aragonite and reprecipitation of calcite along a thin fluid film, at virtually the same place and time (Frisia et al., 2002; Maliva et al., 2009; Zhang et al., 2014). Experimental work suggests that the process of creating/preserving pseudomorphs is rate-limited by the dissolution of the parent material (here: aragonite) rather than by the precipitation of the secondary phase and solute transport to the reaction front (Casella et al., 2017; Putnis & Putnis, 2007). A similar process was indirectly suggested by different authors based on microscopic work on speleothems. When pore fluids become locally, at nanoscale to microscale, saturated in aragonite during ongoing calcite precipitation, aragonite dissolution may slow down or temporarily stop and a relic may become enclosed in the calcite crystal (Martín-García et al., 2014; Martín-Pérez et al., 2012), such as observed here. A detailed speleothem study by Martín-García et al. (2014) and observations of Holocene travertine and tufa by Rodríguez-Berriguete (2020) further suggest that

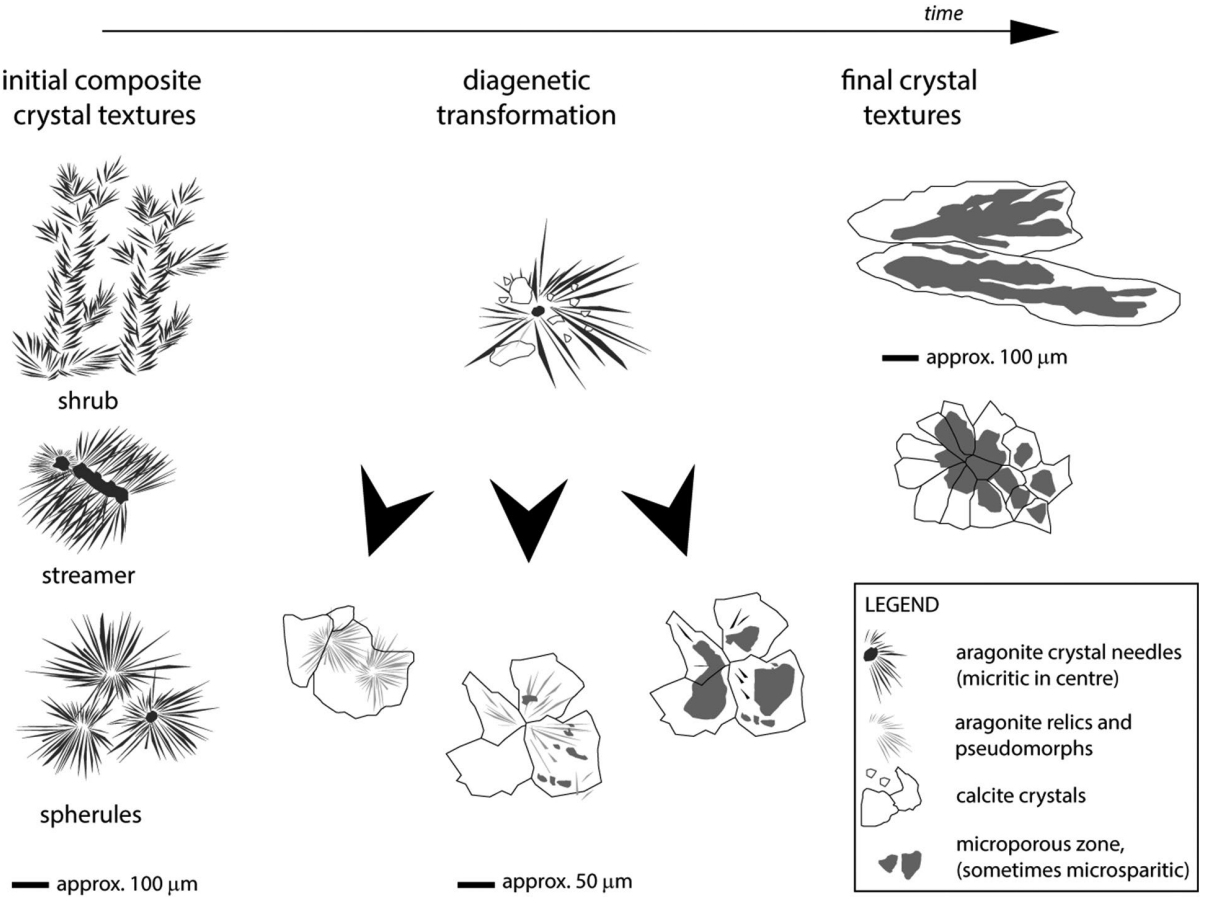

FIGURE 12 Schematic diagram showing how aragonite needles and the composite crystal structures they form change throughout progressive diagenesis as observed at Mammoth Hot Springs and in the Y-10 core

precipitation of calcite started as microcrystalline, scattered crystals between aragonite fibres. The number of calcite crystals then grows and crystals merge, a process referred to as aggrading recrystallization by Rodríguez-Berriguete (2020). This process eventually results in a coarse crystalline mosaic of calcite crystals, with or without enclosed aragonite relics (Martín-García et al., 2014; Rodríguez-Berriguete, 2020; Figure 12).

The appearance of microporosity after neomorphism of aragonite to calcite would suggest that aragonite dissolution proceeds faster than the precipitation and growth of calcite crystals. As more material is dissolved and can be transported away from the reaction front, this may locally create microscopic pore space (Casella et al., 2017). Alternatively, the post-depositional fluid may not have been continuously oversaturated with respect to calcite, leading to dissolution of the metastable aragonite, or only partial neomorphism to, for example, microsparitic calcite.

The origin of micron-sized porosity within ancient travertine deposits has been questioned (Chafetz, 2013; Soete et al., 2014). Extrapolating from observations by Bosak et al. (2004), micropores might be a biosignature, indicating the former physical presence (now holes) or involvement of microorganisms in travertine precipitation. Living microorganisms are abundant in the springs and, in places, play a role in precipitation of $CaCO_3$ (Arp et al., 2010; Kandianis et al., 2008; Rogerson et al., 2008; Shiraishi et al., 2008). The microporosity observed here (Figure 7C,D), however, develops during neomorphism of metastable aragonite and cementation by low magnesium calcite. In aragonitic mollusc shells, which are denser, the expulsion of enclosed organic matter (OM) steers the neomorphism reaction front (Pederson et al., 2019). An increase in microporosity in such calcitic fabrics has not been reported. In experiments where less tight aragonitic fabrics (fluid-buffered system) were exposed to hydrothermal conditions to simulate diagenetic transformations (Pederson et al., 2020), OM was easily removed during the earliest stage of neomorphism/recrystallization. A similar process could be expected to have happened to the travertine samples studied here. OM, OM bound water and/or other impurities thus may have been a driver in localising the initiation of aragonite dissolution. The formation of intracrystalline microporosity more likely relates to small-scale, differential rates of aragonite dissolution and calcite cementation during neomorphism.

Both textures, that is, the presence of aragonite relics or ghosts and the presence of cloudy, microporous crystal cores, occur at distances on the order of tens of microns from each other in single specimens. Such isolation emphasises that in time, and in space, diagenetic processes in spring carbonates were heterogeneous and took place in micro-realms (Golubić et al., 2008).

To conclude, the diagenetic changes that impact the primary fabrics at MHS, that is, neomorphism, overgrowth and cementation, seem to result in homogenization (Guo & Riding, 1994) and coarsening (Rainey & Jones, 2007), often reducing primary (intercrystalline) porosity and leading to a 'convergence' of microscopic fabrics (De Boever et al., 2017a; Golubić et al., 2008; Martín-García et al., 2014). The diagenetic microfabric of cloudy crystals in composite dendrite textures or spherulites has been described from a range of fossil, continental deposits including cool to hot spring environments in different geodynamic and environmental contexts (Arp et al., 2013; Claes et al., 2015, 2017; Gandin & Capezzuoli, 2014; Guo & Riding, 1994). While the fine-grained micritic fabric has, in some cases, been related to precipitation in association with microorganisms or to diagenetic, dissolution related, spar micritization, the observations from MHS show that such textures may result from neomorphism of primary, aragonitic textures. This has implications regarding the interpretation of the mineralogy of ancient carbonate spring deposits, now mostly all calcite, and the chemical characteristics of the source waters.

5.3 | Early diagenesis and the fate of stable isotope signatures

The combination of bulk carbon and oxygen isotopes and spot analyses using micro-SIMS of sub-Recent and fossil travertine shed further light on the diagenetic processes and history of fluid circulation. When looking at the bulk stable isotope values, the carbon–oxygen isotope covariance for both recent and fossil deposits remains virtually the same, and nearly parallel. The offset between the Y-10 core samples and sub-Recent MHS samples is 1–1.5‰ for $\delta^{13}C$. This is within the range of 1-2‰ difference for carbon between the two polymorphs (Swart, 2015).

In active hot spring carbonate deposits, a combination of CO_2 degassing, temperature decrease and evaporation resulting in the increase of $\delta^{13}C$ and $\delta^{18}O$ values downstream has been used to explain carbon–oxygen isotope covariation (Arp et al., 2001; Fouke et al., 2000; Kele et al., 2011; Pentecost, 2005). The isotopic ratios of the older, calcitic deposits preserve this positive trend. The bulk values suggest that aragonite, and later calcite, largely precipitated from the same source fluids over a similar temperature range.

The correlation of the travertine isotopic signature and its position along the downstream outflow path (facies), as documented for the modern deposits (Fouke et al., 2000), are, however, lost in the ancient counterparts. Resetting during neomorphism and calcite precipitation must have blurred the primary downstream trend. Temperature, evaporation, degree of CO_2 degassing and water composition vary not only downstream, but also through time (Fouke et al., 2000; Veysey et al., 2008) with changing spring activity, chemistry, day–night and weather conditions. These changes influence calcite-aragonite stability and the isotopic signal of the carbonates that precipitate

(Gutjahr et al., 1996a, 1996b; Morse, 2002; Morse et al., 2007; Shiraishi et al., 2020). The isotopic value of neomorphosed-cemented travertine would then obviously change, but still vary roughly along the same $\delta^{13}C$–$\delta^{18}O$ trend. The framework of Recent travertine (Figure 3A–D) is rather open and unlikely to have inhibited the percolation of spring waters through the already deposited travertine in the subsurface. This is in agreement with the findings of Sturchio (1990) who concluded, based on the Mg, Sr and Ba content of aragonite and calcite travertine at MHS, that polymorphic transformation must have happened under conditions of high water–rock ratio.

5.4 | Fluid history as revealed by SIMS analyses

Spot analyses of individual calcite phases further reveal the multi-stage fluid history. Micro-SIMS analyses of a modern travertine sample (79% aragonite) show that Cc-1 calcite cementing and replacing aragonitic shrub textures have a variable $\delta^{13}C$ value. Both $\delta^{13}C$ and $\delta^{18}O_{VPDB}$ values are also lower than the bulk isotopic value. These spot analyses in a Recent sample actually fall not on, but off the positive $\delta^{13}C$–$\delta^{18}O_{VPDB}$ trend documented by the bulk values. The results of the Cc-1 spot analyses thus suggest that early neomorphism and cementation of aragonite shrub textures by calcite have not only been induced by the spring waters themselves, but probably also by interference with rain water and CO_2 dissolved from the degradation of OM. This may happen at the surface, for example, during exposure as the result of a drop in spring activity and outflow (Shiraishi et al., 2020), or locally within the travertine as a result of preferential flow due to porosity–permeability heterogeneity (Claes et al., 2017; De Boever et al., 2016; Rodríguez-Berriguete, 2020). A comparable trend is seen in cloudy crystals analysed in sample 38 (Figure 11G–I).

In the core samples, Cc-1 and particularly Cc-2 cements reveal isotopic signatures that are closer to, or a little below the bulk values. Their luminescence is predominantly dull, but may show darker or lighter zones. Both phases make up the bulk cements of most samples and are interpreted to result from spring fluids comparable to those that initiated travertine precipitation, as explained above.

However, the signature of the Mc-1 phase, a micritic rim observed in several samples following Cc1 and Cc-2, is anomalous. This thin micritic rim was difficult to analyse using micro-SIMS due to its fine-grained texture, but the limited number of good quality results show a similar to lower $\delta^{18}O_{VPDB}$ value and 4–6‰ lower values for $\delta^{13}C$ compared to the bulk value, Cc-1 and/or Cc-2 cements. This may point to the calcification and fossilization of what formerly was an encrusting biofilm, coating the pore space. Although the isotopic values are clear and significantly different, an organic or microbial origin could not be further confirmed by microscopic analyses. Calcified EPS has only been observed in modern deposits (Apron-Channel facies) between aragonite needles (Figure 5A). Biofilms are a common feature in, for example, cave deposits (Jones, 2010). Given the omnipresent microbial life at MHS, cryptic OM, including mats, could have been present and it is not unlikely that their calcification resulted in the fine-grained micritic bands observed here.

The Cc-3 cement phase points to a shift in diagenetic fluids. The occurrence of this cement chiefly near the top of the core, as poikilotopic crystals, showing alternating dissolution-precipitation events in cathodoluminescence, suggests the rapidly changing chemical conditions typical of a near-surface open system. The variation in carbon isotopes with more stable $\delta^{18}O_{VPDB}$ values points to diagenesis in meteoric conditions, where rain/snow (lower $\delta^{18}O_{VPDB}$) or evaporative waters (elevated $\delta^{18}O_{VPDB}$ values) infiltrate and carbon derived from CO_2 from the decomposition of OM becomes incorporated in variable amounts. The data points are limited, but samples from the top of the core also suggest an inverted J-trend typical of the so-called meteoric diagenesis (Allan & Matthews, 1982).

5.5 | History and timing of travertine deposition revisited

Travertine ages were revisited to assess (a) the history and possibly the onset of travertine formation and (b) to approximate the timing of complete aragonite to calcite neomorphism.

Three facts hamper interpretation of the results. First, the allowed core sampling density and the small sample size did not allow continuous XRD characterisation and dating of samples. Second, transformation of aragonite to calcite (neomorphism), cementation and dissolution affected all core samples over the entire core length. It is well-known that processes such as dissolution–reprecipitation and neomorphism can remobilise uranium and cause significant leaching leading to age uncertainties and inversions (Bajo et al., 2016; Claes et al., 2020; Frisia et al., 2018; Gutjahr et al., 2013; Scholz et al., 2014). As discussed before, the system has been open and diagenesis can be expected to have reset the uranium concentrations and U/Th ratios. Petrography of recent travertine has also shown that neomorphism and cementation started at the surface, only just after, and, locally, during ongoing precipitation in active springs. Diagenesis may have affected the uranium concentrations and U/Th ratios, but introduced an error inferior to the dating error. Third, travertine deposits have high detrital thorium concentrations rendering age corrections more uncertain. For these reasons, the results have to be interpreted as rough approximations and minimum ages. Focus is therefore more on relative trends, than on absolute values.

The accumulation rates deduced from ΔU/Th dates vary between 2 and 20 mm/year. Such rates are inferior to those

measured in the active Mammoth springs by precipitation experiments, which are on the order of 0.2–1.0 mg/cm^{3}h or ≤5 mm/day (Fouke, 2011; Kandianis et al., 2008). They are, however, higher than values found for banded travertine in fissure ridges at Futamata (0.06 mm/year; Shiraishi et al., 2020) and at different locations in Turkey (Altunel & Karabacak, 2005; Mesci et al., 2008) or for tufa deposits in Spain (average 0.7 mm/year; Rodríguez-Berriguete et al., 2018). In situ measurements at Mammoth were taken over a couple of days in an active stream. Fossil ages also cover periods in which the spring or parts of the outflow path may have been dry. The latter ages therefore could provide a realistic idea of the range of long-term accumulation rates in spring systems, in addition to peak values measured in the flow path of active springs. The maximum age found for the travertine sample at 44.3 m depth (YS28), that is, near the bottom of the continuous travertine section, varies between 13.4 ka ± 1.51 ka and 17.9 ka ± 0.95 ka. These dates are older than those previously reported and may suggest that travertine deposition had already started just before the Holocene. However, the age discrepancies and anomalous $\delta^{234}U_i$ signal of the sample complicate a definitive interpretation.

The U/Th results of this study assign the travertine deposits underlying the Jurassic sandstones to a younger age than the deepest part of the continuous travertine section above. In addition, the sample analysed here has much higher uranium concentrations than the other samples (Table 3). This can either be explained by higher uranium availability from pore water during growth or due to an open system and post-growth uranium uptake. Petrographically, this travertine sample is entirely similar to the travertine above. However, the core section exposes several thin and thicker breccia horizons below, within and above the deeper travertine deposits. These breccia samples disconnect the deeper travertine horizon from the continuous travertine section. They are further absent higher up in the core. Finally, a gap of 1.8 m separates the Jurassic, marine sandstones that cap the deeper travertine section from the top continuous travertine section. While these sandstones are not diamictite deposits (cf. Chafetz & Guidry, 2003), they are clearly marine in origin and have been interpreted as deposits belonging to the Ellis Group. Alternatively, this dating anomaly could be a result of faulting that displaced part of the travertine deposits and/or Mesozoic basement below the continuous travertine section. Faults have been mapped in the region by White et al. (1975; Figure 1), although the exact nature and history of displacements along these faults have not been addressed. This explanation for the dating anomaly suggests recent activity along such structural discontinuities after travertine deposition started in the region during the Holocene/late Pleistocene. It could be further addressed during regional mapping in the area.

Mineralogical analyses demonstrated that at depths around 10 m, aragonite disappears from the system as all aragonite is converted to calcite (Table 1). One sample (YS22) at a depth of 12.74 m has been dated with a corrected age of 3.95 ± 0.19 ka, showing that the polymorphic transformation of aragonite to calcite at the location of the Y-10 core was completed in that time window. This window is longer than the 9 ± 0.2 year calculated by Sturchio (1990), which was based on a comparison between the $^{228}Ra/^{226}Ra$ ages of an aragonitic sample from the active Angel Terrace spring and currently exposed deposits at an inactive spring (MHS-24) that are completely calcitic. Estimations of aragonite to calcite inversion rates under wet conditions and temperatures <100°C range widely (De Boever et al., 2017a; Frisia et al., 2002; Zhang et al., 2014). A recent very detailed study by Zhang et al. (2014) on aragonite–calcite speleothems demonstrates neomorphism in less than 8.9 ka using U–Th ages. Budd (1988) report complete inversion in 5–16 ka in phreatic, meteoric diagenetic environments. However, hot spring deposits in Italy were found to completely invert in 15 days (Malesani & Vannucchi, 1975). These variations in aragonite-calcite inversion rates depend largely on the permeability of the deposits, the physicochemical conditions (T, water composition) of the fluids that aragonite deposits have been exposed to and that drive the inversion reaction (Bischoff & Fyfe, 1968; Casella et al., 2017). The approximation of rates for neomorphism in this study is in general agreement with rates found in other studies where inversion is also driven by waters similar to those involved in primary precipitation (Budd, 1988; Frisia et al., 2002; Zhang et al., 2014). The rates, however, seem longer than those inferred for active hot spring deposits (Malesani & Vannucchi, 1975; Sturchio, 1990).

6 | CONCLUSIONS

Spring systems are very efficient and fast precipitating non-marine calcium carbonate factories. However, many fabrics in older, Quaternary, but also more recent deposits suggest diagenetic overprinting. Clear ideas on the diagenetic pathways, products, impact on geochemical and palaeoclimatological signatures and the rates of these processes are still scarce. In this study, the Y-10 core that was drilled in 1967 at one of the upper terraces of the MHS in YNP (USA) was revisited and compared to observations of active spring deposits, with the goal to shed light on the nature, impact and timing of early diagenesis in (hot) spring carbonates.

The Y-10 core reveals a sequence of continuous travertine deposition (around 50 m) overlying Mesozoic siltstones, conglomerates, marine sandstones and limestones. The travertine depositional facies in the upper 50 m of the core show a rough distal to proximal trend upwards confirming observations by Chafetz and Guidry (2003). Bulk stable carbon and oxygen isotope values show a positive $\delta^{13}C$-$\delta^{18}O_{VPDB}$ trend ($\delta^{13}C$: 2.6–4.8‰, $\delta^{18}O_{VPDB}$: −27.3 to −21.2‰), similar to that of

modern travertine deposits in nearby springs, but a distal to proximal trend in the bulk isotope values is not present in the fossil deposits.

Low-resolution to high-resolution microscopy shows that diagenesis has already started in modern springs. The sequence of diagenetic phases is observed in the core regardless of the depositional facies and tends to homogenise depositional fabrics. Petrography and stable isotope spot analyses using micro-SIMS allow two main episodes to be distinguished in terms of fluid circulation:

1. Open system circulation of the spring waters through the heterogeneous but often porous primary spring fabrics results in neomorphism of aragonite, creation of microporosity within the calcite crystals (Cc-1, Cc-2), fossilization of potential microbial mats in cavities (Mc-1) and calcite cementation and dissolution. The driving fluids are often the same as those that induced the initial calcium carbonate precipitation. Early diagenesis therefore leads to a resetting of the isotope signature, but preserves the $\delta^{13}C$-$\delta^{18}O$ covarying trend as a function of temperature and fluid composition, of the modern spring deposits.
2. Open system circulation of fluids leads to late stage dissolution and cementation by a well-zoned non-luminescent to bright and dull luminescent calcite (Cc-3), predominantly at the top of the core. Uniform $\delta^{18}O_{VPDB}$ values and a range of lower $\delta^{13}C$ values suggest the influence of infiltrating meteoric fluids.

The diagenetic changes that impact the primary fabrics at MHS, that is, neomorphism, overgrowth and cementation, seem to result in a homogenization and coarsening of microfabrics in spring carbonates, significantly reducing its primary porosity. In this study, SIMS analyses proved to be a powerful technique in determining the stable isotope signature of individual cement generations. These often diverted from the bulk values that were measured and therefore allowed better detangling of the fluid history and changing precipitation conditions during diagenesis.

The interpretation of U/Th ages of two modern and four Y-10 core travertine samples is complicated by the elevated level of (detrital) thorium. The new ages acquired in this study suggest that travertine deposition at the MHS location started at the very end of the Pleistocene/beginning Holocene. If differences between ages of samples at different depths are approximately preserved, a range of depositional rates between 2 and 20 mm/year can be deduced. Aragonite completely disappears from the record at depths of 10 m, suggesting that neomorphism is completed before 3.95 (±0.19) ka. The deposits underlying the continuous travertine sequence have been interpreted by Sturchio (1990) as clastic interlayers, glacial till and Mesozoic basement. These deposits were interpreted as volcanoclastic sediments in the study of Chafetz and Guidry (2003). They are re-assigned in this study to different deposits of Mesozoic age and to possible fault breccia. Fault displacement after the onset of travertine deposition is further considered responsible for the presence of travertine deposits below rocks that belong to the Late Jurassic marine sandstone unit of the Swift Formation (Ellis Group). It could explain why the age of this small travertine unit in the core is younger than the lowermost sample dated in the continuous travertine section above.

ACKNOWLEDGEMENTS

Funding for the first author, the microscopic and analytical work was provided by SNSF (Ambizione Project 154810 QuantiCarb@Spring). David Jaramillo-Vogel was funded through the project 4D-Diagenesis@Mound (SNSF grant 200021_14924). Total E&P (Project n_FR5585) allowed field work and thin section preparation. Special thanks go to the staff of the USGS Core Research Center (CRC) Denver for allowing access and assisting in sampling of the Y-10 core and also to the Yellowstone National Park staff (permit n_YELL-2014-SCI-3060) for supporting this research. Fouke is acknowledged for having helped to organise sample permission at Yellowstone National Park and for the enriching discussions during the preparation stages of the project. Dr. Laura DeMott (Syracuse University, USA) and Msc Anja-Sara Koestinger (University of Fribourg, Switzerland) are acknowledged for their assistance during core description. René Eichstädter is acknowledged for U/Th dating. We are grateful to Herman Nijs (KU Leuven, Belgium) for the preparation of thin sections and to Prof. Dr. M. Joachimski (GeoZentrum Nordbayern, Erlangen, Germany) for the stable isotope analyses of bulk powder samples. Christophe Neururer is thanked for support with the SEM facilities and Prof. Bernard Grobéty for providing access to the XRD facilities at the University of Fribourg. Spot analyses of stable carbon and oxygen isotopes were conducted at the micro-SIMS instrument, part of the SwissSIMS facilities and the platform CASA (University of Lausanne, Switzerland). At last, we thank two anonymous reviewers, the editors of the journal and the special issue for their careful and much appreciated review and comments.

DATA AVAILABILITY STATEMENT

Data and images of the Y-10 core that support the findings of this study are openly available through the webpage of the USGS CRC Denver at https://my.usgs.gov/crcwc/core/report/11629.

ORCID


Eva De Boever https://orcid.org/0000-0002-7514-4936

REFERENCES

Allan, J.R. & Matthews, R.K. (1982) Isotope signatures associated with early meteoric diagenesis. *Sedimentology*, *29*, 797–817.10.1111/j.1365-3091.1982.tb00085.x

Altunel, E. & Karabacak, V. (2005) Determination of horizontal extension from fissure-ridge travertines: A case study from the Denizli Basin, southwestern Turkey. *Geodinamica Acta*, *18*, 333–342.

Andrews, J.E. (2006) Palaeoclimatic records from stable isotopes in riverine tufas: Synthesis and review. *Earth-Science Reviews*, *75*, 85–104. https://doi.org/10.1016/j.earscirev.2005.08.002

Andrews, J.E. & Brasier, A.T. (2005) Seasonal records of climatic change in annually laminated tufas: Short review and future prospects. *Journal of Quaternary Science*, *20*, 411–421. https://doi.org/10.1002/jqs.942

Arp, G., Bissett, A., Brinkmann, N., Cousin, S., de Beer, D., Friedl, T., Mohr, K.I., Neu, T.R., Reimer, A., Shiraishi, F., Stackebrandt, E. & Zippel, B. (2010) Tufa-forming biofilms of German karstwater streams: Microorganisms, exopolymers, hydrochemistry and calcification. In: Pedley, H.M. & Rogerson, M. (Eds.) *Tufas and speleothems: Unravelling the microbial and physical controls*. London: Geological Society, pp. 83–118.

Arp, G., Kolepka, C., Simon, K., Karius, V., Nolte, N. & Hansen, B.T. (2013) New evidence for persistent impact-generated hydrothermal activity in the Miocene Ries impact structure, Germany. *Meteoritics & Planetary Science*, *48*, 2491–2516. https://doi.org/10.1111/maps.12235

Arp, G., Wedemeyer, N. & Reitner, J. (2001) Fluvial tufa formation in a hard-water creek (Deinschwanger Bach, Franconian Alb, Germany). *Facies*, *44*, 1–22. https://doi.org/10.1007/BF02668163

Bajo, P., Hellstrom, J., Frisia, S., Drysdale, R., Black, J., Woodhead, J., Borsato, A., Zanchetta, G., Wallace, M.W., Regattieri, E. & Haese, R. (2016) "Cryptic" diagenesis and its implications for speleothem geochronologies. *Quaternary Science Reviews*, *148*, 17–28. https://doi.org/10.1016/j.quascirev.2016.06.020

Bargar, K.E. (1978) Geology and thermal history of Mammoth Hot Springs, Yellowstone National Park, Wyoming. *Geological Survey Bulletin*, *1444*, 1–55.

Bischoff, J.L. & Fyfe, W.S. (1968) Catalysis, inhibition and the calcite-aragonite problem. I. The aragonite-calcite transformation. *American Journal of Science*, *266*, 80–90.

Bissett, A., Reimer, A., De Beer, D., Shiraishi, F. & Arp, G. (2008) Metabolic microenvironmental control by photosynthetic biofilms under changing macroenvironmental temperature and pH conditions. *Applied and Environment Microbiology*, *74*, 6306–6312. https://doi.org/10.1128/AEM.00877-08

Boch, R., Leis, A., Haslinger, E., Goldbrunner, J.E., Mittermayr, F., Fröschl, H., Hippler, D. & Dietzel, M. (2017) Scale-fragment formation impairing geothermal energy production: Interacting H2S corrosion and $CaCO_3$ crystal growth. *Geothermal Energy*, *5*, 4. https://doi.org/10.1186/s40517-017-0062-3

Bosak, T., Souza-Egipsy, V., Corsetti, F.A. & Newman, D.K. (2004) Micrometer-scale porosity as a biosignature in carbonate crusts. *Geology*, *32*, 781–784. https://doi.org/10.1130/G20681.1

Brasier, A.T. (2011) Searching for travertines, calcretes and speleothems in deep time: Processes, appearances, predictions and the impact of plants. *Earth-Science Reviews*, *104*, 213–239. https://doi.org/10.1016/j.earscirev.2010.10.007

Brasier, A.T., Andrews, J.E. & Kendall, A.C. (2011) Diagenesis or dire genesis? The origin of columnar spar in tufa stromatolites of central Greece and the role of chironomid larvae. *Sedimentology*, *58*, 1283–1302.

Brasier, A.T., Andrews, J.E., Marca-Bell, A.D. & Dennis, P.F. (2010) Depositional continuity of seasonally laminated tufas: Implications for δ18O based palaeotemperatures. *Global and Planetary Change*, *71*, 160–167. https://doi.org/10.1016/j.gloplacha.2009.03.022

Brasier, A.T., Rogerson, M.R., Mercedes-Martín, R., Vonhof, H.B. & Reijmer, J.J.G. (2015) A test of the biogenicity criteria established for microfossils and stromatolites on quaternary tufa and Speleothem materials formed in the "Twilight Zone" at Caerwys, UK. *Astrobiology*, *15*, 883–900. https://doi.org/10.1089/ast.2015.1293

Brogi, A., Capezzuoli, E., Aqué, R., Branca, M. & Voltaggio, M. (2009) Studying travertines for neotectonics investigations: Middle-Late Pleistocene syn-tectonic travertine deposition at Serre di Rapolano (Northern Apennines, Italy). *International Journal of Earth Sciences*, *99*, 1383–1398. https://doi.org/10.1007/s00531-009-0456-y

Budd, D.A. (1988) Aragonite-to-calcite transformation during freshwater diagenesis of carbonates: Insights from pore-water chemistry. *GSA Bulletin*, *100*, 1260–1270.

Casella, L.A., Griesshaber, E., Yin, X., Ziegler, A., Mavromatis, V., Müller, D., Ritter, A.C., Hippler, D., Harper, E.M., Dietzel, M., Immenhauser, A., Schöne, B.R., Angiolini, L. & Schmahl, W.W. (2017) Experimental diagenesis: Insights into aragonite to calcite transformation of *Arctica islandica* shells by hydrothermal treatment. *Biogeosciences*, *14*, 1461–1492. https://doi.org/10.5194/bg-14-1461-2017

Chafetz, H.S. (2013) Porosity in bacterially induced carbonates: Focus on micropores. *American Association of Petroleum Geologists Bulletin*, *97*, 2103–2111. https://doi.org/10.1306/04231312173

Chafetz, H.S. & Guidry, S.A. (2003) Deposition and diagenesis of mammoth Hot Springs travertine, Yellowstone National Park, Wyoming, USA. *Canadian Journal of Earth Sciences*, *40*, 1515–1529. https://doi.org/10.1139/E03-051

Chafetz, H.S., Srdoc, D. & Horvatincic, N. (1994) Early diagenesis of Plitvice Lakes waterfall and barrier travertine deposits. *Géographie Physique et Quaternaire*, *48*, 247–255.

Cheng, H., Edwards, R.L., Hoff, J., Gallup, C.D., Richards, D.A. & Asmerom, Y. (2000) The half-lives of uranium-234 and thorium-230. *Chemical Geology*, *169*, 17–33. https://doi.org/10.1016/S0009-2541(99)00157-6

Christiansen, R.L. (1999) Digital geologic map for Yellowstone National Park, Idaho, Montana, and Wyoming and Vicinity. Open-File Report, 99–0174.

Claes, H., Marques-Erthal, M., Soete, J., Özkul, M. & Swennen, R. (2017) Shrub and pore type classification: Petrography of travertine shrubs from the Ballık-Belevi area (Denizli, SW Turkey). *Quaternary International*, *217*, 147–163.

Claes, H., Soete, J., Van Noten, K., El Desouky, H., Erthal, M.M., Vanahecke, F., Özkul, M. & Swennen, R. (2015) Sedimentology, 3D geobody reconstruction and CO_2-source delineation of travertine palaeo-deposits in the Ballık area. *Sedimentology*, *62*, 1408–1445. https://doi.org/10.1111/sed.12188

Claes, H., Török, A., Soete, J., Mohammadi, Z., Vassilieva, E., Hamaekers, H., Erthal, M., Aratman, C., Cheng, H., Edwards, R.L. Shen, C.C., Özkul, M., Kele, S., Minszenty, A. & Swennen, R. (2020) U/Th dating and open system behaviour of travertine. *Quaternaire*, *31*, 117–132.

De Boever, E., Brasier, A.T., Foubert, A. & Kele, S. (2017a) What do we really know about early diagenesis of non-marine carbonates? *Sedimentary Geology*, *361*, 25–51. https://doi.org/10.1016/j.sedgeo.2017.09.011

De Boever, E., Foubert, A., Lopez, B., Swennen, R., Jaworowski, C., Özkul, M. & Virgone, A. (2017b) Comparative study of the Pleistocene Cakmak quarry (Denizli Basin, Turkey) and modern Mammoth Hot Springs deposits (Yellowstone National Park, USA).

Quaternary International, *437*, 129–146. https://doi.org/10.1016/j.quaint.2016.09.011

De Boever, E., Foubert, A., Oligschlaeger, D., Claes, S., Soete, J., Bertier, P., Özkul, M., Virgone, A. & Swennen, R. (2016) Quantification of porosity in continental spring carbonate facies – Case study from plugs of the Cakmak quarry (Denizli, Turkey). *Geochemistry, Geophysics, Geosystems*, *17*, 2922–2939.

Della Porta, G. (2015). Carbonate build-ups in lacustrine, hydrothermal and fluvial settings: Comparing depositinoal geometry, fabric types and geochemical signature. In: Bosence, D.W.J., Gibbons, K.A., Le Heron, D.P., Morgan, W.Q., Pritchard, T. & Vining, B.A. (Eds.), *Microbial carbonates in space and time: Implications for global exploration and production*. *Geological Society of London, Special Publications*, *418*, 17–68.

Della Porta, G., Capezzuoli, E. & De Bernardo, A. (2017) Facies character and depositional architecture of hydrothermal travertine slope aprons (Pleistocene, Acquasanta Terme, Central Italy). *Marine and Petroleum Geology*, *87*, 171–187. https://doi.org/10.1016/j.marpetgeo.2017.03.014

Dickson, J.A.D. (1978) Neomorphism and recrystallization. In: Middleton, G.V., Church, M.J., Coniglio, M., Hardie, L.A. & Longstaffe, F.J. (Eds.) *Encyclopedia of sediments and sedimentary rocks. Encyclopedia of earth sciences series*. Dordrecht: Springer, pp. 753–757. https://doi.org/10.1007/978-1-4020-3609-5_143

Douville, E., Paterne, M., Cabioch, G., Louvat, P., Gaillardet, J., Juillet-Leclerc, A. & Ayliffe, L. (2010) Abrupt sea surface pH change at the end of the Youner Dryas in the central sub-equatorial Pacific inferred from boron isotope abundance in corals (Porites). *Biogeosciences*, *7*, 2445–2459.

Falk, E.S., Guo, W., Paukert, A.N., Matter, J.M., Mervine, E.M. & Kelemen, P.B. (2016) Controls on the stable isotope compositions of travertine from hyperalkaline springs in Oman: Insights from clumped isotope measurements. *Geochimica et Cosmochimica Acta*, *192*, 1–28. https://doi.org/10.1016/j.gca.2016.06.026

Flügel, E. (2004) *Microfacies of carbonate rocks: Analysis, interpretation and application*. Berlin, Heidelberg: Springer-Verlag. ISBN: 978-3-642-03796-2. https://doi.org/10.1007/978-3-642-03796-2

Folk, R.L. (1965) Some aspects of recrystallization in ancient limestones. *SEPM (Society for Sedimentary Geology) Special Publication*, *13*, 14–48.

Fouke, B.W. (2011) Hot-spring systems geobiology: Abiotic and biotic influences on travertine formation at Mammoth Hot Springs, Yellowstone National Park, USA. *Sedimentology*, *58*, 170–219. https://doi.org/10.1111/j.1365-3091.2010.01209.x

Fouke, B.W., Bonheyo, G.T., Sanzenbacher, B. & Frias-lopez, J. (2003) Partitioning of bacterial communities between travertine depositional facies at Mammoth Hot Springs, Yellowstone National Park, USA. *Canadian Journal of Earth Sciences*, *40*, 1531–1548. https://doi.org/10.1139/E03-067

Fouke, B.W., Farmer, J.D., Des Marais, D.J., Pratt, L., Sturchio, N.C., Burns, P.C. & Discipulo, M.K. (2000) Depositional facies and aqueous-solid geochemistry of travertine-depositing hot springs (Angel Terrace, Mammoth Hot Springs, Yellowstone National Park, U.S.A.). *Journal of Sedimentary Research Section A. Sedimentary Petrology and Processes*, *70*, 565–585.

Fraser, G.D., Waldrop, H.A. & Julius Hyden, H. (1969) Geology of the Gardiner Area Park County Montana. *Geological Survey Bulletin*, *1277*, 1–118.

Frisia, S., Borsato, A., Fairchild, I.J., Mcdermott, F. & Selmo, E.M. (2002) Aragonite-calcite relationships in speleothems (Grotte De Clamouse, France): Environment, fabrics, and carbonate geochemistry. *Journal of Sedimentary Research*, *72*, 687–699. https://doi.org/10.1306/020702720687

Frisia, S., Borsato, A. & Hellstrom, J. (2018) High spatial resolution investigation of nucleation, growth and early diagenesis in speleothems as exemplar for sedimentary carbonates. *Earth-Science Reviews*, *178*, 68–91. https://doi.org/10.1016/j.earscirev.2018.01.014

Gagrcía-del-Cura, M.Á., Benavente, D., Marínez-Martínez, J. & Cueto, N. (2012) Sedimentary structures and physical properties of travertine and carbonate tufa building stone. *Construction and Building Materials*, *28*, 456–467.

Gandin, A. & Capezzuoli, E. (2014) Travertine: Distinctive depositional fabrics of carbonates from thermal spring systems. *Sedimentology*, *61*, 264–290.

Golubić, S., Violante, C., Plenković-Moraj, A. & Grgasović, T. (2008) Travertines and calcareous tufa deposits: An insight into diagenesis. *Geologia Croatica*, *61*, 363–378.

Guo, L. & Riding, R. (1994) Origin and diagenesis of Quaternary travertine shrub fabrics, Rapolano Terme, eastern Italy. *Sedimentology*, *41*, 499–520.

Guo, L. & Riding, R. (1998) Hot-spring travertine facies and sequences, Late Pleistocene, Rapolano Terme, Italy. *Sedimentology*, *45*, 163–180.

Guo, L. & Riding, R. (1999) Rapid facies changes in Holocene fissure ridge hot spring travertines, Rapolano Terme, Italy. *Sedimentology*, *46*, 1145–1158. https://doi.org/10.1046/j.1365-3091.1999.00269.x

Gutjahr, A., Dabringhaus, H. & Lacmann, R. (1996a) Studies of the growth and dissolution kinetics of the $CaCO_3$ polymorphs calcite and aragonite II. The influence of divalent cation additives on the growth and dissolution rates. *Journal of Crystal Growth*, *158*, 310–315.

Gutjahr, A., Dabringhaus, H. & Lacmann, R. (1996b) Studies of the growth and dissolution kinetics of the $CaCO_3$ polymorphs calcite and aragonite I. Growth and dissolution rates in water. *Journal of Crystal Growth*, *158*, 296–309.

Gutjahr, M., Vance, D., Hoffmann, D.L., Hillenbrand, C.D., Foster, G.L., Rae, J.W.B. & Kuhn, G. (2013) Structural limitations in deriving accurate U-series ages from calcitic cold-water corals contrast with robust coral radiocarbon and Mg/Ca systematics. *Chemical Geology*, *355*, 69–87. https://doi.org/10.1016/j.chemgeo.2013.07.002

Janssen, A., Swennen, R., Podoor, N. & Keppens, E. (1999) Biological and diagenetic influence in Recent and fossil tufa deposits from Belgium. *Sedimentary Geology*, *126*, 75–95. https://doi.org/10.1016/S0037-0738(99)00033-0

Jones, B. (2010) Microbes in caves: Agens of calcite corrosion and precipitation. In: Pedley, H.M. & Rogerson, M. (Eds.), *Tufas and speleothems: Unravelling the microbial and physical controls*. *Geological Society of London, Special Publication, London*, *336*, 7–30.

Jones, B. (2017) Review of aragonite and calcite crystal morphogenesis in thermal spring systems. *Sedimentary Geology*, *354*, 9–23. https://doi.org/10.1016/j.sedgeo.2017.03.012

Jones, B. & Peng, X. (2012) Intrinsic versus extrinsic controls on the development of calcite dendrite bushes, Shuzhishi Spring, Rehai geothermal area, Tengchong, Yunnan Province, China. *Sedimentary Geology*, *249*, 45–62. https://doi.org/10.1016/j.sedgeo.2012.01.009

Jones, B. & Renaut, R.W. (2008) Cyclic development of large, complex, calcite dendrite crystals in the Clinton travertine, Interior British Columbia, Canada. *Sedimentary Geology*, *203*, 17–35. https://doi.org/10.1016/j.sedgeo.2007.10.002

Jones, B. & Renaut, R.W. (2010) Calcareous spring deposits in continental settings. In: Alonso-Zarza, A.M. & Tanner, L. (Eds.) *Carbonates*

in continental settings. Amsterdam: Elsevier, pp. 177–224. https://doi.org/10.1016/S0070-4571(09)06104-4

Kandianis, M.T., Fouke, B.W., Johnson, R.W., Veysey, J. & Inskeep, W.P. (2008) Microbial biomass: A catalyst for $CaCO_3$ precipitation in advection-dominated transport regimes. *Bulletin of the Geological Society of America*, *120*, 442–450. https://doi.org/10.1130/B26188.1

Kano, A., Matsuoka, J., Kojo, T. & Fujii, H. (2003) Origin of annual laminations in tufa deposits, southwest Japan. *Palaeogeography, Palaeoclimatology, Palaeoecology*, *191*, 243–262. https://doi.org/10.1016/0031-0182(02)00717-4

Kele, S., Özkul, M., Fórizs, I., Gökgöz, A., Baykara, M.O., Alçiçek, M.C. & Németh, T. (2011) Stable isotope geochemical study of Pamukkale travertines: New evidences of low-temperature non-equilibrium calcite-water fractionation. *Sedimentary Geology*, *238*, 191–212. https://doi.org/10.1016/j.sedgeo.2011.04.015

Kele, S., Vaselli, O., Szabó, C. & Minissale, A. (2003) Stable isotope geochemistry of Pleistocene travertine from Budakalász (Buda Mts, Hungary). *Acta Geologica Hungarica*, *46*, 161–175. https://doi.org/10.1556/AGeol.46.2003.2.4

Kharaka, Y.K., Mariner, R.H., Bullen, T.D., Kennedy, B.M. & Sturchio, N.C. (1991) Geochemical investigations of hydraulic connections between Corwin springs known geothermal area and adjacent parts of Yellowstone National Park. In: *Effects of potential geothermal development in the Corwin Springs known geothermal resources Area, Montana, on the thermal featers of Yellowstone National Park*. Menlo Park, CA: US Geological Survey, pp. F1–F38. Available at: https://www.geothermal-library.org/index.php?mode=pubs&action=view&record=1018923

Kharaka, Y.K., Sorey, M.L. & Thordsen, J.J. (2000) Large-scale hydrothermal fluid discharges in the Norris-Mammoth corridor, Yellowstone National Park, USA. *Journal of Geochemical Exploration*, *69–70*, 201–205. https://doi.org/10.1016/S0375-6742(00)00025-X

Lohmann, K.C. (1988) Geochemical patterns of meteoric diagenetic systems and their application to studies of paleokarst. In: James, N.P. & Choquette, P.W. (Eds.) *Paleokarst*. New York: Springer-Verlag, pp. 58–78.

Lopez, B., Camoin, G., Özkul, M., Swennen, R. & Virgone, A. (2017) Sedimentology of coexisting travertine and tufa deposits in a mounded geothermal spring carbonate system, Obruktepe, Turkey. *Sedimentology*, *64*, 903–931. https://doi.org/10.1111/sed.12284

Lowenstern, J.B. & Hurwitz, S. (2008) Monitoring a supervolcano in repose: Heat and volatile flux at the Yellowstone caldera. *Elements*, *4*, 35–40.

Ludwig, K.R. & Titterington, D.M. (1994) Calculation of 230Th/U isochrons, ages, and errors. *Geochimica et Cosmochimica Acta*, *58*, 5031–5042 10.1016/0016-7037(94)90229-1 .

Malesani, P. & Vannucchi, S. (1975) Precipitazione di calcite o i aragonite dalle acque termominerale in relazione alla genesi e all'evoluzione dei travertini. *Atti della Accademia Nazionale dei Lincei. Classe di Scienze Fisiche, Matematiche e Naturali*, *58*, 761–766.

Maliva, R.G., Missimer, T.M., Clayton, E.A. & Dickson, J.A.D. (2009) Diagenesis and porosity preservation in Eocene microporous limestones, South Florida, USA. *Sedimentary Geology*, *217*, 85–94. https://doi.org/10.1016/j.sedgeo.2009.03.011

Martín-García, R., Alonso-Zarza, A.M. & Martín-Pérez, A. (2009) Loss of primary texture and geochemical signatures in speleothems due to diagenesis: Evidences from Castañar Cave, Spain. *Sedimentary Geology*, *221*, 141–149. https://doi.org/10.1016/j.sedgeo.2009.09.007

Martín-García, R., Alonso-Zarza, A.M., Martín-Pérez, A., Schröder-Ritzrau, A. & Ludwig, T. (2014) Relationships between colour and diagenesis in the aragonite-calcite speleothems in Basajaún Etxea cave, Spain. *Sedimentary Geology*, *312*, 63–75. https://doi.org/10.1016/j.sedgeo.2014.08.001

Martín-Pérez, A., Martín-García, R. & Alonso-Zarza, A.M. (2012) Diagenesis of a drapery speleothem from Castañar Cave: From dissolution to dolomitization. *International Journal of Speleology*, *41*, 251–266. https://doi.org/10.5038/1827-806X.41.2.11

Mesci, B.L., Gürsoy, H. & Tatar, O. (2008) The evolution of travertine-masses in the Sivas Area (Central Turkey) and their relationships to active tectonics. *Turkish Journal of Earth Sciences*, *17*, 219–240.

Moore, C.H. & Wade, W.J. (2013) *Carbonate reservoirs, porosity and diagenesis in a sequence stratigraphic framework*, 2nd edition. Amsterdam: Elsevier.

Morse, J.W. (2002) The dissolution kinetics of major sedimentray carbonate minerals. *Earth-Science Reviews*, *58*, 51–84.

Morse, J.W., Arvidson, R.S. & Lüttge, A. (2007) Calcium carbonate formation and dissolution. *Chemical Reviews*, *107*, 342–381. https://doi.org/10.1021/cr050358j

Okumura, T., Takashima, C. & Kano, A. (2013) Textures and processes of laminated travertines formed by unicellular cyanobacteria in myoken hot spring, southwestern Japan. *Island Arc*, *22*, 410–426. https://doi.org/10.1111/iar.12034

Okumura, T., Takashima, C., Shiraishi, F., & Kano, A. (2012) Textural transition in an aragonite travertine formed under various flow conditions at Pancuran Pitu, Central Java, Indonesia. *Sedimentary Geology*, *265–266*, 195–209. https://doi.org/10.1016/j.sedgeo.2012.04.010

Pederson, C.L., Mavromatis, V., Dietzel, M., Rollion-Bard, C., Breitenbach, S.F.M., Yu, D., Nehrke, G. & Immenhauser, A. (2020) Variation in the diagenetic response of aragonite archives to hydrothermal alteration. *Sedimentary Geology*, *406*, 105716. https://doi.org/10.1016/j.sedgeo.2020.105716

Pederson, C., Mavromatis, V., Dietzel, M., Rollion-Bard, C., Nehrke, G., Jöns, N., Jochum, K.P. & Immenhauser, A. (2019) Diagenesis of mollusc aragonite and the role of fluid reservoirs. *Earth and Planetary Science Letters*, *514*, 130–142. https://doi.org/10.1016/j.epsl.2019.02.038

Peng, X. & Jones, B. (2013) Patterns of biomediated $CaCO_3$ crystal bushes in hot spring deposits. *Sedimentary Geology*, *294*, 105–117. https://doi.org/10.1016/j.sedgeo.2013.05.009

Pentecost, A. (1990) The formation of travertine shrubs: Mammoth hot springs, Wyoming. *Geological Magzine*, *127*, 159–218.

Pentecost, A. (2005) *Travertine*. Berlin, Heidelberg: Springer-Verlag.

Putnis, A. & Putnis, C.V. (2007) The mechanism of re-equilibration of solids in the presence of a fluid phase. *Journal of Solid State Chemistry*, *180*, 1783–1786.

Rainey, D.K. & Jones, B. (2007) Rapid cold water formation and recrystallization of relict bryophyte tufa at the Fall Creek cold springs, Alberta, Canada. *Canadian Journal of Earth Sciences*, *44*, 889–909. https://doi.org/10.1139/E07-008

Rodríguez-Berriguete, Á. (2020) Early diagenetic features in Holocene travertine and tufa from a volcanic setting (Azuaje, Gran Canaria, Spain). *Facies*, *66*, 1–16. https://doi.org/10.1007/s10347-020-00602-z

Rodríguez-Berriguete, Á., Alonso-Zarza, A.M., Martín-García, R., del Cabrera, M.C. (2018) Sedimentology and geochemistry of a human-induced tufa deposit: Implications for palaeoclimatic research. *Sedimentology*, *65*, 2253–2277. https://doi.org/10.1111/sed.12464

Rogerson, M., Pedley, H.M., Wadhawan, J.D. & Middleton, R. (2008) New insights into biological influence on the geochemistry of freshwater carbonate deposits. *Geochimica et Cosmochimica Acta*, *72*, 4976–4987. https://doi.org/10.1016/j.gca.2008.06.030

Ruppel, E.T. (1982) Geology of pre-tertiary rocks in the northern part of Yellowstone National Park, Wyoming. Thirty-Third Annual Field Conference Yoming Geological Association Guidebook. Denver, CO: USGS, pp. 111–137.

Rye, R.O. & Truesdell, A.H. (2007) The question of recharge to the deep thermal reservoir underlying the geysers and hot springs of Yellowstone National Park. In: Morgan, L.A. (Ed.), *Integrated geoscience studies in the greater yellowstone area – Volcanic, tectonic, and hydrothermal processes in the yellowstone ecosystem*. US Geological Survey, pp. 235–270.

Scholz, D., Tolzmann, J., Hoffmann, D.L., Jochum, K.P., Spötl, C. & Riechelmann, D.F.C. (2014) Diagenesis of speleothems and its effect on the accuracy of 230Th/U-ages. *Chemical Geology*, *387*, 74–86. https://doi.org/10.1016/j.chemgeo.2014.08.005

Sharp, I., Verwerk, K., Ferreira, H., Lapponi, F., Snidero, M., Machado, V., Holtar, E., Swart, R., Marsch, J., Gindre, L., Puigdefabregas, C. & Fejerskov, M. (2013) Pre- and post-salt non-marine carbonates of the Namibe Basin, Angola. In: Bosence, D., Gibbons, K., Le Heron, D. P., Morgan, W. A., Pritchard, T. & Vining, B. A. (Eds.) *Microbial carbonates in space and time: Implications for global exploration and production*. London: The Geological Society of London, pp. 52–53.

Shiraishi, F., Bissett, A., de Beer, D., Reimer, A. & Arp, G. (2008) Photosynthesis, respiration and exopolymer calcium-binding in biofilm calcification (Westerhöfer and Deinschwanger Creek, Germany). *Geomicrobiology Journal*, *25*, 83–94. https://doi.org/10.1080/01490450801934888

Shiraishi, F., Morikawa, A., Kuroshima, K., Amekawa, S., Yu, T.L., Shen, C.C., Kakizaki, Y., Kano, A., Asada, J. & Bahniuk, A.M. (2020) Genesis and diagenesis of travertine, Futamata hot spring, Japan. *Sedimentary Geology*, *405*, 105706. https://doi.org/10.1016/j.sedgeo.2020.105706

Soete, J., Huysmans, M., Claes, H., Claes, S., Özkul, M. & Swennen, R. (2014) Petrophysical and geostatistical analysis of porosity-permeability and occurrence of facies types in continental carbonates of the Ballık area, Denizli (Turkey). In: *Reservoir quality of clastic and carbonate rocks: Analysis, modelling and prediction*. London: The Geological Society. Conference abstract, pp. 166–167.

Soete, J., Kleipool, L.m., Claes, H., Claes, S., Hamaekers, H., Kele, S., Özkul, M., Foubert, A., Reijmer, J. & Swennen, R. (2015) Acoustic properties in travertines and their relation to porosity and pore types. *Marine and Petroleum Geology*, *59*, 320–335. https://doi.org/10.1016/j.marpetgeo.2014.09.004

Sorey, M.L. & Colvard, E.M. (1997) Hydrologic investigations in the Mammoth Corridor, Yellowstone National Park and vicinity, U.S.A. *Geothermics*, *26*, 221–249. https://doi.org/10.1016/S0375-6505(96)00041-7

Sturchio, N.C. (1990) Radium isotopes, alkaline earth diagenesis, and age determination of travertine from Mammoth Hot Springs, Wyoming, U.S.A. *Applied Geochemistry*, *5*, 631–640.

Sturchio, N.C., Pierce, K.L., Murrell, M.T. & Sorey, M.L. (1994) Uranium-series ages of travertines and timing of the last glaciation in the Northern Yellowstone area, Wyoming-Montana. *Quaternary Research*, *41*, 265–277.

Swart, P.K. (2015) The geochemistry of carbonate diagenesis: The past, present and future. *Sedimentology*, *62*, 1233–1304. https://doi.org/10.1111/sed.12205

Takashima, C. & Kano, A. (2008) Microbial processes forming daily lamination in a stromatolitic travertine. *Sedimentary Geology*, *208*, 114–119. https://doi.org/10.1016/j.sedgeo.2008.06.001

Titschack, J., Goetz-Neuhoeffer, F. & Neubauer, J. (2011) Magnesium quantification in calcites [(Ca, Mg)CO_3] by Rietveld-based XRD analyses: Revisiting a well-established method. *American Mineralogist*, *96*, 1028–1038.

Török, Á., Mindszenty, A., Claes, H., Kele, S., Fodor, L. & Swennen, R. (2016) Geobody architecture of continental carbonates: "Gazda" travertine quarry (Süttö, Gerecse Hills, Hungary). *Quaternary International*, *437*, 1–22 10.1016/j.quaint.2016.09.030

Veysey, J., Fouke, B.W., Kandianis, M.T., Schickel, T.J., Johnson, R.W. & Goldenfeld, N. (2008) Reconstruction of water temperature, pH, and flux of ancient hot springs from travertine depositional facies. *Journal of Sedimentary Research*, *78*, 69–76. https://doi.org/10.2110/jsr.2008.013

Wefing, A.-M., Arps, J., Blaser, P., Wienberg, C., Hebbeln, D. & Frank, N. (2017) High precision U-series dating of scleractiinian cold-water corals using an automated chromatographic U and Th extraction. *Chemical Geology*, *475*, 140–148.

White, D.E., Fournier, R., Muffler, L.F.P. & Truesdell, A.H. (1975) Physical results of research drilling in thermal areas of Yellowstone National, Wyoming. Geological Survey Professional Paper 892. Washington

Zhang, H., Cai, Y., Tan, L., Qin, S. & An, Z. (2014) Stable isotope composition alteration produced by the aragonite-to-calcite transformation in speleothems and implications for paleoclimate reconstructions. *Sedimentary Geology*, *309*, 1–14. https://doi.org/10.1016/j.sedgeo.2014.05.007

Zhang, P., Zhang, N., Liu, Y., Lu, Y.T., Kan, A.T. & Tomson, M.B. (2018) Application of a novel tube reactor for investigation of calcium carbonate mineral scale deposition kinetics. *Chemical Engineering Research and Design*, *137*, 113–124. https://doi.org/10.1016/j.cherd.2018.07.001

SUPPORTING INFORMATION

Additional supporting information may be found online in the Supporting Information section.

How to cite this article: De Boever E, Jaramillo-Vogel D, Bouvier A-S, et al. The fate of a travertine record: Impact of early diagenesis on the Y-10 core (Mammoth Hot Springs, Yellowstone National Park, USA). *Depositional Rec*. 2022;8:220–250. https://doi.org/10.1002/dep2.143